ELSEVIER

Tectonophysics 324 (2000) 137–168

TECTONOPHYSICS

www.elsevier.com/locate/tecto

Temperature-dependent viscoelastic compaction and compartmentalization in sedimentary basins

J.A.D. Connolly*, Yu.Yu. Podladchikov

Department of Earth Sciences, Swiss Federal Institute of Technology, Sonneggstrasse 5, CH-8092 Zurich, Switzerland

Received 25 January 2000; accepted for publication 28 February 2000

Abstract

The near-surface compaction regime of most sedimentary basins is characterized by hydrostatic fluid pressures and is therefore determined entirely by sediment matrix rheology. Within this regime, compaction is initially well described by a pseudoelastic rheological model. With increasing depth, precipitation–dissolution processes lead to thermally activated viscous deformation. The steady-state porosity profile of the viscous regime is a function of two length scales; the viscous e-fold length, related to the compaction activation energy; and a scale determined by the remaining parameters of the sedimentary process. Overpressure development is weakly dependent on the second scale for activation energies >20 kJ/mol. Application of the steady-state model to Pannonian basin shales and sandstones indicates a dominant role for viscous compaction in these lithologies at porosities below 10 and 25%, respectively. Activation energies and shear viscosities derived from the profiles are 20–40 kJ/mol and 10^{20}–10^{21} Pa-s at 3 km depth. The analytical formulation of the compaction model provides a simple method of predicting both the depth at which permeability limits compaction, resulting in top-seal formation, and the amount of fluid trapped beneath the top-seal. Fluid flow during hydraulically limited compaction is unstable such that sedimentation rate perturbations or devolatilization cause nucleation of porosity waves on the viscous e-fold length scale, ~ 0.5–1.5 km. The porosity waves are characterized by fluid overpressure with a hydrostatic fluid pressure gradient and propagate through creation of secondary porosity in response to the mean stress gradient. The waves are a mechanism of episodic fluid expulsion that can be significantly more efficient than uniform Darcyian fluid flow, but upward wave propagation is constrained by the compaction front so that the waves evolve into essentially static domains of high porosity following cessation of sedimentation. Yielding mechanisms do not appreciably alter the time and length scale of episodic fluid flow, because fluid expulsion is ultimately controlled by compaction. The flow instabilities inherent in viscous compaction are similar to, and a possible explanation for, fluid compartments.

Keywords: devolatilization; fluid compartments; porosity waves; sedimentary basins; viscoelastic compaction

1. Introduction

High-porosity domains of overpressured pore fluid are a ubiquitous feature of sedimentary basins (e.g. Hunt, 1990; Powley, 1990). The fluid pressure gradient within these domains or ‘fluid compartments’ is near to hydrostatic, and the domains are bounded by relatively impermeable seals. The detailed structure of a fluid compartment beneath the uppermost ‘top seal’ is generally complex, typically consisting of a series of sub-compartments within which the mean fluid pressure

---

* Corresponding author. Tel.: +41-1-632-7804; fax: +41-1-632-1088.

E-mail address: jamie@erdw.ethz.ch (J.A.D. Connolly)

0040-1951/00/$ - see front matter
PII: S0040-1951(00)00084-6

approaches lithostatic pressure with increasing depth. The geometry and scale of the compartments are often entirely controlled by geologic structure or lithologic heterogeneity. However, in many basins, the top seal occurs at approximately constant depth and shows only local correlation to structure and lithology (e.g. Hunt, 1990; Al-Shaieb et al., 1994; Surdam et al., 1994). In these cases, the depth of onset for fluid overpressures is ~ 3 km and appears to show some relation to the geothermal gradient. These observations suggest that compartmentalization may be intrinsically related to sedimentary compaction and, in particular, thermally activated features of compaction, a hypothesis that is examined here with a one-dimensional mathematical model of the compaction process.

Most studies of compaction driven fluid flow in sedimentary basins presume that porosity is a known function of distance from the sediment–water interface, thus they model the consequences of compaction rather than the compaction process itself. Sedimentary compaction at shallow depth is by rotation and crushing of the sediment grains. Although this mechanism results in a plastic rheology, if reasonable assumptions are made about the deformation path, a pseudoelastic model can describe the compaction process (e.g. Shi and Wang, 1986; Audet and Fowler, 1992; Wangen, 1992). These models can explain overpressure development in a pre-existing compartment in response to perturbations caused by processes such as heating or devolatilization, but are usually inadequate to explain seal formation and compartmentalization (Kooi, 1997). With increasing depth and temperature, compaction occurs largely by dissolution–precipitation processes (e.g. Lundegard, 1992; Qin and Ortoleva, 1994; Bjørkum, 1995). Because the resulting deformation is time-dependent and irreversible, the rheology is viscous. Dissolution–precipitation processes are incompletely understood, but are generally thought to result in thermally activated linear viscous rheology (e.g. Angevine and Turcotte, 1983; Rutter, 1983; Schneider et al., 1996). Steady sedimentation of a matrix with thermally activated viscous rheology was investigated numerically by Schneider et al. (1996), but analytical treatments discount thermal activation (e.g. Sumita et al., 1996; Fowler and Yang, 1999), an important limitation in the context of low-temperature, near-surface environments. Accordingly, this paper begins with the presentation and parameterization of a steady-state mathematical formulation to account for thermally activated compaction that is then verified by comparison to transient numerical calculations and applied to a natural example.

Steady fluid flow through a viscous matrix is unstable, such that perturbations that create an obstruction to upward fluid flow induce fluid-filled porosity waves (Richter and McKenzie, 1984; Scott and Stevenson, 1984). Porosity waves are self-propagating domains of overpressured porosity. McKenzie (1987) briefly considered the development of porosity waves in the context of sedimentary basins and argued that the rapid deposition of sediments onto a partially compacted sediment layer would initiate waves. More thorough analysis shows that the waves are more likely to initiate in response to a reduction in sedimentation rate (Sumita et al., 1996). Regardless of this detail, the observation that fluid compartments are common in rapidly accumulated sedimentary sequences (e.g. Hunt, 1990) provides a compelling argument for the relevance of McKenzie's model. However, the assumption of constant matrix viscosity creates a cosmetic flaw in that the waves propagate upward rapidly. The waves are therefore incapable of forming compartments that would persist on the time scale of sedimentation, a characteristic of sedimentary fluid compartments demonstrated by the presence of mature hydrocarbons. McKenzie's model might be reconciled with the observation that top seal formation is, at least sometimes, related to temperature, if thermally activated mineral precipitation were capable of forming an obstruction to the upward propagation of porosity waves (e.g. Hunt, 1990; Aharanov et al., 1997). Equilibrium transport of saturated solutes is inadequate to create obstructions because of low solubility gradients (e.g. Connolly and Thompson, 1989; Robinson and Gluyas, 1992). Consequently, it is necessary to invoke disequilibrium phenomena to explain flow obstructions by mineral precipitation. Mechanisms of disequilibrium seal formation exploit local lithologic heterogeneity (e.g. Birchwood and Turcotte, 1994; Qin and Ortoleva, 1994; Oelkers et al., 1996) but, on a mesoscopic scale, are equivalent to viscous compaction as considered here. Under metamorphic conditions, viscous compaction with temperature-dependent rheology leads to the formation of essentially static one-dimensional porosity waves (Connolly, 1997; Connolly and Podladchikov, 1998). In the second part of this paper, we seek to establish whether such waves are likely to form on significant time and length scales in sedimentary basins as a result of compaction or diagenetic devolatilization.

Porosity waves are a mechanism of fluid flow in which porosity dilation and compaction propagates a domain of high porosity toward conditions of lower mean stress, i.e. in most cases upward. In prior studies of viscous compaction, it has been assumed that matrix viscosity is independent of the sign of the effective pressure. This assumption implies that the negative effective pressure responsible for pore dilation must be comparable in magnitude to the positive effective pressure that induces compaction at depth. It is improbable that sediments support large negative effective pressures without yielding (e.g. Bjørlykke and Hoeg, 1997). We implement a viscoplastic model in which pore compaction and dilation are viscous and plastic, respectively, to account for this possibility.

2. Mathematical formulation and parameterization

We consider Darcyian flow of an incompressible fluid through a viscoelastic sediment matrix composed of incompressible solid grains. Although the solid and fluid components are incompressible, the sediment is compressible because fluid may be expelled from the pore volume. Conservation of solid and fluid mass requires:

$$\frac{\partial(1-\phi)}{\partial t}+\nabla((1-\phi)v_{\mathrm{s}})=0 \tag{1}$$

and

$$\frac{\partial\phi}{\partial t}+\nabla(\phi v_{\mathrm{f}})=0, \tag{2}$$

where ϕ is porosity, and subscripts f and s distinguish the velocities, v, of the fluid and sediment (see Table 1 for notation). The force balance between the matrix and fluid is by Darcy's law:

$$\phi(v_{\mathrm{f}}-v_{\mathrm{s}})=-\frac{k}{\mu}\nabla\bar{p}, \tag{3}$$

where: k is the matrix permeability; μ is the fluid viscosity, which, in view of the large variation possible in permeability, we consider constant; $\bar{p}$ is the fluid overpressure defined relative to hydrostatic conditions such that $\bar{p}=p_{\mathrm{f}}-\rho_{\mathrm{f}}gz$, with downward increasing depth coordinate, z; and ρ_{f} is the fluid density. The sediment matrix rheology is introduced through Terzaghi's effective stress principle for a Maxwell viscoelastic bulk rheology:

$$\nabla v_{\mathrm{s}}=-\phi\left(\frac{p_{\mathrm{e}}}{\zeta}+\beta\frac{\mathrm{d}p_{\mathrm{e}}}{\mathrm{d}t}\right), \tag{4}$$

where p_{e} is the effective pressure, β and ζ are the coefficients of bulk matrix compressibility and viscosity, and $\mathrm{d}/\mathrm{d}t=(\partial/\partial t+v_{\mathrm{s}}\nabla)$ is the material derivative of the sediment properties. The effective pressure is the difference between the mean stress and the fluid pressure, i.e. $p_{\mathrm{e}}=\bar{\sigma}-p_{\mathrm{f}}$. The porosity dependence of the rheological equation is necessitated by the requirement that the matrix must become incompressible as $\phi\rightarrow 0$. This dependence follows directly from the first-order non-zero terms of a Taylor series expansion of ∇v_{s} as a function of ϕ, p_{e}, and $\mathrm{d}p_{\mathrm{e}}/\mathrm{d}t$; thus, we refer to the simplest rheology in which β and ζ are independent of porosity as a linear viscoelastic rheology. Non-linear rheology results if β and ζ are dependent on porosity, a possibility that we explore subsequently for the viscous term. The near-surface compaction of sediment is plastic, but if the sediment load increases monotonically, plastic and elastic formulations are mathematically equivalent (Audet and Fowler, 1992; Wangen, 1992; Fowler and Yang, 1998). We therefore adopt Eq. (4) to describe plastic compaction, which we designate as pseudo-elastic to differentiate the physical process from truly reversible elastic behavior. The coefficient, β, is then the coefficient of the effective pore compressibility during monotonic loading, i.e. the

Table 1
Common symbols and characteristic parameter values[a]

Symbol	Meaning	Units	Typical value
De	Local Deborah number, Eqs. (20) and (30)		
k, k_r	Permeability, Eq. (21); reference value at ϕ_r	m^2	10^{-13}–10^{-21}
l	Viscous e-fold length, Eq. (27)	m	500–1500 m
m	Bulk viscosity porosity exponent, Eq. (23)		0–1
n	Permeability porosity exponent, Eq. (21)		3
p_f, p_e	Fluid pressure; effective pressure, $\rho_s gz - p_f$	Pa	
$\bar{p}$	Overpressure, $p_f - \rho_f gz$	Pa	
Q	Creep activation energy, Eq. (25)	kJ/mol	20–70
q_s	Sediment (sedimentation rate) flux	m/My	10^1–10^3
S_f, S_ϕ	Fluid and porosity source terms	m^3/m^3-s	Eq. (65)
T, T_r	Temperature; reference value, Eq. (25)	K	473
t	Time	s or My	
v_f, v_s	Fluid and sediment velocity	m/My	
v_ϕ	Porosity phase velocity	m/My	
z, z_r	Depth; reference value for η_r, Eq. (26)	m	3000
z_c	Depth of top seal formation, Eq. (38)	m	2000–4000
β	Coefficient of pore compressibility	Pa^{1-}	10^{-8}
κ	Hydraulic constant, Eq. (41)		Fig. 5
λ_c	Rheological constant, Eq. (32)	m	Fig. 5
ϕ, ϕ_r	Porosity; reference value for k, Eq. (21)		25%
ϕ_c, ϕ_{ss}	Top seal and fluidization porosity, Fig. 2		Eq. (40), Eq. (46)
ϕ_0, ϕ_1	Porosity at onset of compaction, Fig. 2		
η, η_r	Sediment shear viscosity, Eq. (25); η at z_r	Pa-s	10^{20}–10^{24}
ζ	Coefficient of sediment bulk viscosity	Pa-s	Eq. (23)
ρ_f, ρ_s, $\Delta\rho$	Fluid density; sediment density; $\rho_s - \rho_f$	kg/m^3	900, 2600, 1700
μ	Fluid shear viscosity	Pa-s	10^{-4}
ω	Local hydraulic parameter, Eqs. (20) and (41)		
^	As superscript, an estimator		

[a] See Fig. 2 for additional notation.

inverse of the tangential bulk hardening modulus in loading.

The mass conservation constraint [Eq. (1)] can be rearranged to express the divergence of the matrix velocity in terms of the material derivative of the porosity:

$$\nabla v_s = \frac{1}{1-\phi}\frac{d\phi}{dt}. \tag{5}$$

Addition of Eqs. (1) and (2) gives the divergence of the total volumetric flux of matter as:

$$\nabla(v_s + \phi(v_f - v_s)) = 0. \tag{6}$$

Eqs. (6) and (3), together with the definition of effective pressure, give:

$$\nabla\left(v_s - \frac{k}{\mu}(\nabla\bar{\sigma} - \rho_f g u_z - \nabla p_e)\right) = 0 \tag{7}$$

where u_z is the unit vector directed toward increasing depth. Eqs. (1), (4), and (7) then form a system of three equations in four unknown quantities $\{\phi, p_e, v_s, \nabla\bar{\sigma}\}$ that becomes closed if $\nabla\bar{\sigma}$ is specified as a function of depth.

2.1. One-dimensional compaction

Sedimentary compaction is primarily a process of sediment consolidation orthogonal to the Earth's gravitational field. We thus approximate the process as one-dimensional. In this context, Eq. (7) may be integrated to express the sediment velocity at depth

$$v_s = q_t + \frac{k}{\mu}\left(\frac{\partial\bar{\sigma}}{\partial z} - \rho_f g - \frac{\partial p_e}{\partial z}\right), \tag{8}$$

where q_t is the total volumetric flux of matter through the sedimentary column. Employing Eq. (5) to express the divergence of the matrix velocity in terms of porosity, Eqs. (4) and (7) are

$$\frac{1}{1-\phi}\frac{d\phi}{dt} = -\phi\left(\frac{p_e}{\zeta} + \beta\frac{dp_e}{dt}\right) \tag{9}$$

$$\frac{1}{1-\phi}\frac{d\phi}{dt} = \frac{\partial}{\partial z}\left(\frac{k}{\mu}\left(\frac{\partial\bar{\sigma}}{\partial z} - \rho_f g - \frac{\partial p_e}{\partial z}\right)\right), \tag{10}$$

where, from Eq. (8), the material derivative is

$$\frac{d}{dt} = \frac{\partial}{\partial t} + \left(q_t + \frac{k}{\mu}\left(\frac{\partial\bar{\sigma}}{\partial z} - \rho_f g - \frac{\partial p_e}{\partial z}\right)\right)\frac{\partial}{\partial z} \tag{11}$$

and $\partial/\partial z$ is the partial derivative in a reference frame defined relative to the sediment–water interface. In truly isostatic compaction, the mean stress gradient is well approximated by the gradient of the sediment load

$$\frac{\partial\bar{\sigma}}{\partial z} = ((1-\phi)\rho_s + \phi\rho_f)g \tag{12}$$

where ρ_s is the solid density. Eq. (12) introduces arithmetic complexity into the compaction equations (cf., Fowler and Yang, 1999) without accounting for the potentially important contribution of deviatoric stresses into the force balance for consolidated sediments. Deviatoric stresses in partially consolidated sediments are sensitive to far-field stresses, basin fill history, topographic slope and rheology. In light of these sources of inaccuracy, we simplify Eq. (12) by taking the mean stress gradient as a constant external parameter such that

$$\frac{\partial\bar{\sigma}}{\partial z} = \rho_s g, \tag{13}$$

where ρ_s becomes the effective density of the sedimentary column. We justify this simplification by the subsequent result that our formulation provides an adequate description of the compaction of near-surface poorly consolidated sediments, where the greatest variations in bulk density occur.

2.1.1. Steady-state compaction

During uniform sedimentation, transient compaction evolves toward a steady-state limit; the time scale of this evolution increases strongly with depth due to the reduction in permeability caused by consolidation. Consequently, for the characteristic sedimentation time, the near-surface regime is expected to be in closer proximity to the steady-state limit. We therefore begin by supposing the existence of a stationary state extending from the sediment–water interface to a depth, z_{ss}, such that the porosity profile is independent of time, a situation often referred to as equilibrium compaction. In the one-dimensional steady state, integration of Eq. (1) gives

$$v_s = \frac{v_{ss}(1-\phi_{ss})}{(1-\phi)} = \frac{q_s}{(1-\phi)} \tag{14}$$

where q_s is the sediment flux $v_0(1-\phi_0)$ at the sediment–water interface, i.e. the sedimentation rate, and subscripts ‘ss’ and ‘0’ denote values at z_{ss} and at $z=0$. Material derivatives then expand as $d/dt = q_s/(1-\phi)\partial/\partial z$. Eq. (9) requires that connection of the steady-state porosity to the more slowly compacting transient regime must occur at conditions such that the effective pressure and its gradient are vanishingly small, i.e. as $z\rightarrow z_{ss}$, $p_e\rightarrow 0$ and $\partial p_e/\partial z\rightarrow 0$. These conditions, together with Eqs. (8) and (13), constrain the total flux to

$$q_t = v_{ss} - \frac{k_{ss}}{\mu}\Delta\rho g \tag{15}$$

with $\Delta\rho = \rho_s - \rho_f$. Using Eq. (14) to express the local sediment velocity, v_s, in terms of v_{ss}, Eqs. (8) and (9) form a closed system of two ordinary differential equations in two unknown functions $\{\phi, p_e\}$

$$\frac{\partial p_e}{\partial z} = \Delta\rho g\left(1 - \frac{k_{ss}}{k}\right) - \frac{\mu v_{ss}}{k}\frac{\phi - \phi_{ss}}{1-\phi} \tag{16}$$

$$\frac{\partial\phi}{\partial z}=-\phi(1-\phi)\left(\frac{p_e}{\zeta q_s}(1-\phi)+\beta\frac{\partial p_e}{\partial z}\right). \tag{17}$$

Defining the dimensionless effective pressure and depth as $p'=p_e/p^*$ and $z'=z/L$, with $p^*=L\Delta\rho g$ and L a measure of the compaction length scale, Eqs. (16) and (17) can be expressed in non-dimensional form as

$$\frac{\partial p'}{\partial z'}=1-\frac{k_{ss}}{k}-\omega\frac{\phi-\phi_{ss}}{1-\phi}\approx 1-\omega\phi \tag{18}$$

$$\frac{\partial\phi}{\partial z'}=-\phi(1-\phi)\beta'\left(\frac{p'}{De}(1-\phi)+\frac{\partial p'}{\partial z'}\right) \tag{19}$$

in terms of three dimensionless parameters

$$\omega=\frac{\mu v_{ss}}{k\Delta\rho g}\approx\frac{\mu q_s}{k\Delta\rho g},\ De=\frac{q_s\beta\zeta}{L},\ \beta'=\beta L\Delta\rho g. \tag{20}$$

The approximation in Eq. (18) holds when the permeability and porosity of the steady-state domain are much larger than in the subjacent transient domain. Eq. (18) gives the effective pressure gradient as a function of ω such that when $\omega \ll 1$ the effective pressure gradient is $\Delta\rho g$, a condition corresponding to a hydrostatic, i.e. normal, fluid pressure gradient. The inverse relationship between sediment velocity and permeability embodied in ω is sometimes used to distinguish regimes of slow $\omega\to 0$ and fast $\omega\to\infty$ compaction (Audet and Fowler, 1992; Wangen, 1992; Fowler and Yang, 1998). The Deborah number, *De* (Judges 5:5; Reiner, 1964), in Eq. (19) is a measure of the relative influence of the viscous and pseudoelastic mechanisms on the shape of the compaction profile, such that when $De\sim 1$, both components are comparable, and $De\to 0$ and $De\to\infty$ represent the viscous and pseudoelastic limits. Both ω and *De* may be strongly dependent on the compaction process; therefore, to complete the formulation, it is necessary to specify the relationships of permeability and bulk viscosity to porosity and depth.

2.2. Porosity–permeability

A non-linear porosity–permeability relationship is a necessary condition for the development of flow instabilities during viscous compaction (e.g. Barcilon and and Richter, 1986). Such a relationship is represented by

$$k=\left(\frac{k_r}{\phi_r^n}\right)\phi^n \tag{21}$$

where k_r is the permeability at a reference porosity, ϕ_r. From theory, permeability is expected to vary as a quadratic or cubic function of the connected porosity (e.g. Gueguen and Dienes, 1989), whereas network modeling of natural pore distributions suggests porosity exponents near three (Zhu et al., 1995). Permeability–porosity trends in clay-rich rocks (Neuzil, 1994; Schneider et al., 1996) are also consistent with a cubic porosity–permeability relationship, and because such lithologies are likely to limit the effective permeability of sedimentary basins, a cubic ($n=3$) porosity–permeability relationship is generally assumed here. Experimentally determined porosity–permeability relationships often have much higher porosity exponents (e.g. $n>10$, David et al., 1994) that may partially reflect transient phenomena that are unimportant on the compaction time scale (Connolly, 1997). In comparison to empirical logarithmic porosity–permeability relationships (e.g. Bethke, 1985; Van Balen and Cloetingh, 1994) used in basin modeling, a cubic function provides for a conservative model. Logarithmic relationships lead to more rapid reduction in permeability with compaction and depth, resulting in overpressuring and undercompaction at shallower depths and higher porosity. Such relationships would amplify flow instabilities that develop from compaction disequilibrium.

The permeability of sediment with 25% porosity, which is taken as ϕ_r, varies from 10^{-12} to 10^{-21} m^2 (e.g. Gueguen and Palciauskas, 1994; Neuzil, 1994; Schneider et al., 1996). Shales and clay-rich rocks define the lower five decades of this spectrum, which grades continuously into values characteristic of sandstones. This spectrum is broader than the ranges often assumed for basin modeling (10^{-12}–10^{-18} m^2, e.g. Bethke, 1985; Van Balen and Cloetingh, 1994), which may be considered more typical.

2.3. Bulk matrix viscosity

There is variation concerning the definition of bulk viscosity and its dependence on porosity. In distinction to works that equate the divergence of the matrix velocity to $-p_e/\zeta$ (e.g. Birchwood and Turcotte, 1994; Schneider et al., 1996; Connolly, 1997; Connolly and Podladchikov, 1998), our formulation gives the viscous compaction rate, obtained by rearrangement of Eq. (9), setting β equal to zero, as

$$\frac{1}{\phi}\frac{\mathrm{d}\phi}{\mathrm{d}t}=-\frac{(1-\phi)}{\zeta}p_e. \tag{22}$$

With this formulation, in the limit of non-interacting pores (e.g. Nye, 1953), the proportionality coefficient, ζ, in Eq. (22) is comparable to the shear viscosity and independent of porosity. We therefore identify this parameter as an analog to the bulk viscosity. Constant ζ is frequently assumed in compaction modeling (e.g. Fowler, 1990; Birchwood and Turcotte, 1994; Sumita et al., 1996). For materials with Newtonian shear viscosity, more complex models of porosity reduction indicate a weak dependence of ζ on porosity such that

$$\zeta\approx\frac{\eta}{\phi^{m-1}} \tag{23}$$

with m between zero and unity (e.g. Scott and Stevenson 1984; Ashby, 1988). Formulations of the compaction equations consistent with our formulation when $m=0$ (e.g. McKenzie, 1984; Schneider et al., 1996; Fowler and Yang, 1999) may be appropriate for pressure solution creep at porosities above 10% (Helle et al., 1985). However, at small porosities, $m<1$ is inconsistent with the non-interacting pore limit and seems unrealistic because the compaction rate becomes infinite, in conflict with intuition that compaction should become increasingly difficult as porosity decreases; moreover, $m\leq 0$ permits the development of negative porosity. In non-Newtonian sediment such as carbonates and evaporites (e.g. Spiers and Schutjens, 1990), at constant effective pressure, ζ is a weakly decreasing function of porosity (e.g. Ashby, 1988)

$$\zeta\propto\frac{(1-\phi^{1/q})^q}{(1-\phi)} \tag{24}$$

where q is identical to the stress exponent in the constitutive equation for the effective shear viscosity. Compaction dictated by such rheologies does not differ in a fundamental way from that of Newtonian shear rheology with $q=1$ (e.g. Connolly, 1997). Accordingly, we assume Newtonian shear rheology and, unless otherwise indicated, constant ζ in Eq. (23), i.e. $m=1$.

Grain-scale dissolution–precipitation processes are sometimes referred to as ‘pressure solution creep’ to distinguish them from ‘chemical compaction’ processes that involve diffusional mass transport on greater length scales ($\sim$0.01–1 m, e.g. Qin and Ortoleva, 1994; Oelkers et al., 1996). Both mechanisms are complex and incompletely understood. To avoid this complexity, the effective sediment shear viscosity is expressed

$$\eta=\eta_r\exp\left(\frac{Q(1-T/T_r)}{\mathrm{R}T}\right) \tag{25}$$

where Q is the creep activation energy, η_r is the viscosity at temperature, T_r. This approach masks potentially important mesoscopic effects caused by lithologic heterogeneity, but captures the essence of the thermally activated character of viscous compaction. To obviate consideration of temperature and activation energy as independent variables, an alternative expression for the shear viscosity is

$$\eta=\eta_r\exp\left(\frac{z_r-z}{l}\right) \tag{26}$$

where η_r is the viscosity at depth z_r, and l is the ‘viscous e-fold length’, the length scale over which the shear viscosity changes by a factor equal to the natural log base (e). For a linear geotherm, comparison of Eqs. (25) and (26) gives (Connolly and Podladchikov, 1998)

$$l=\frac{\mathrm{R}T^2}{Q\nabla T}. \tag{27}$$

Experimental data suggest that activation energies of 20–70 kJ/mol are appropriate for pressure solution creep in sedimentary rocks (e.g. Shimizu, 1995; Schneider et al., 1996). For geothermal gradients $\nabla T = 25$–150 K/km, these activation energies give e-fold lengths of 500–3000 m at a depth of 3 km (Fig. 1a). Because the e-fold length is not a strong function of depth, the error introduced by assuming a constant e-fold length over a depth interval of $\sim 5l$ is minor, but generally leads to a more rapid decrease in viscosity above z_r and a less rapid decay at depth. The effect of varying either the geothermal gradient or the activation energy can be assessed from calculations for different e-fold lengths. Numerical calculations here based upon Eq. (26) are for a geothermal gradient of 50 K/km with Q equal to either 20 or 60 kJ/mol, which correspond to values of l equal to 1500 and 500 m with $z_r = 3000$ m.

For normal fluid pressures, i.e. $p_e = \Delta\rho g z$, the local time scale, τ, required for an e-fold decrease in porosity, from Eqs. (22) and (26), is

$$\tau = \left(\frac{\mathrm{d}\ln\phi}{\mathrm{d}t}\right)^{-1} = \frac{(1-\phi)\eta_r}{\phi^{m-1} z\Delta\rho g}\exp\left(\frac{z_r - z}{l}\right). \qquad (28)$$

Taking l as a measure of the length scale over which the time scale is relevant, with $m = 1$, the velocity that a particular level of porosity propagates upward by compaction under normally pressured conditions is independent of the porosity and given by

$$\hat{v}_\phi = -\frac{l}{\tau} = -\frac{zl\Delta\rho g}{\eta_r}\exp\left(\frac{z - z_r}{l}\right) \qquad (29)$$

where $\hat{v}_\phi$ is used to distinguish the approximation from the true phase velocity, v_ϕ. Because $-\hat{v}_\phi$ increases rapidly with depth, during viscous compaction, a stationary porosity profile can be expected to develop in which downward porosity advection is compensated by compaction, such

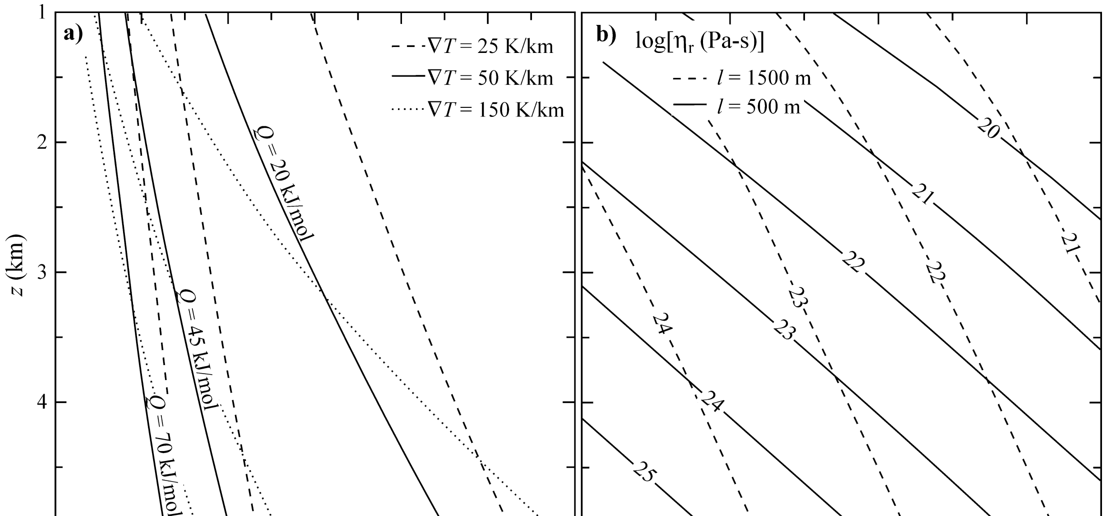

Fig. 1. (a) Viscous e-fold length (l, Eq. (27)) as a function of depth, activation energy and geothermal gradient. (b) Approximate viscous compaction velocity [$\hat{v}_\phi$, Eq. (29)] for hydrostatic fluid pressure as a function of z, l, and η_r (with $m = 1$ and parameters as in Table 1). If $\hat{v}_\phi < v_s$, then porosity is advected downward by burial; the maximum depth to which porosity can be advected without the development of fluid overpressure is that at which $-\hat{v}_\phi = v_s$. Maintenance of normal pressures to 3 km depth therefore requires $\eta_r = 10^{21}$–10^{23} Pa-s for sedimentation rates of 10–10^3 m/My. If sedimentation ceases, $\hat{v}_\phi$ approximates the velocity of the compaction front toward the surface; preservation of normally pressured sedimentary porosity profiles on a geological time scale therefore requires short viscous e-fold lengths, i.e. a strong temperature dependence of viscous compaction.

that the porosity at any depth remains constant, i.e. $-v_\phi = q_s/(1-\phi)$. Incipient overpressuring at 3 km depth as a consequence of viscous compaction therefore constrains η_r to 10^{20}–10^{24} Pa-s (Fig. 1b) for plausible time-averaged sedimentation rates (10–3000 m/My; e.g. Audet, 1996; Kooi, 1997). Likewise, for normal fluid pressures, Eq. (26) gives the local Deborah number [Eq. (20)] as

$$De = \frac{q_s \eta_r \beta}{z\phi^{m-1}} \exp\left(\frac{z - z_r}{l}\right), \qquad (30)$$

which gives the maximum width of the transition between pseudoelastic and viscous compaction as $\sim 2l$ for $m \le 1$. It follows that if the near-surface compaction regime is pseudoelastic, overpressure development by viscous dominated compaction at 3 km depth requires values of $l < 1500$ m. Preservation of sedimentary porosity profiles once sedimentation ceases is difficult to explain if porosity phase velocities do not decay somewhat more rapidly surfaceward than estimated for $l = 1500$ (Fig. 1b), an observation that supports our thesis that viscous compaction in sedimentary basins is thermally activated.

3. Quasi-steady-state compaction

Elementary consideration admits two limiting compaction regimes (Fig. 2) dependent on the local value of ω [Eq. (20); Wangen, 1992; Audet and Fowler, 1992; Fowler and Yang, 1998], which is a strong function of porosity through Eq. (21). If $\omega \ll 1$, then negligible deviations from hydrostatic fluid pressure are necessary to accommodate compaction-generated fluid fluxes, and compaction is dictated entirely by rheology [Eq. (9) or (17)]. Because normal fluid pressures imply a linear increase in effective pressure with depth, the rheologically limited regime gives rise to an interval of rapid

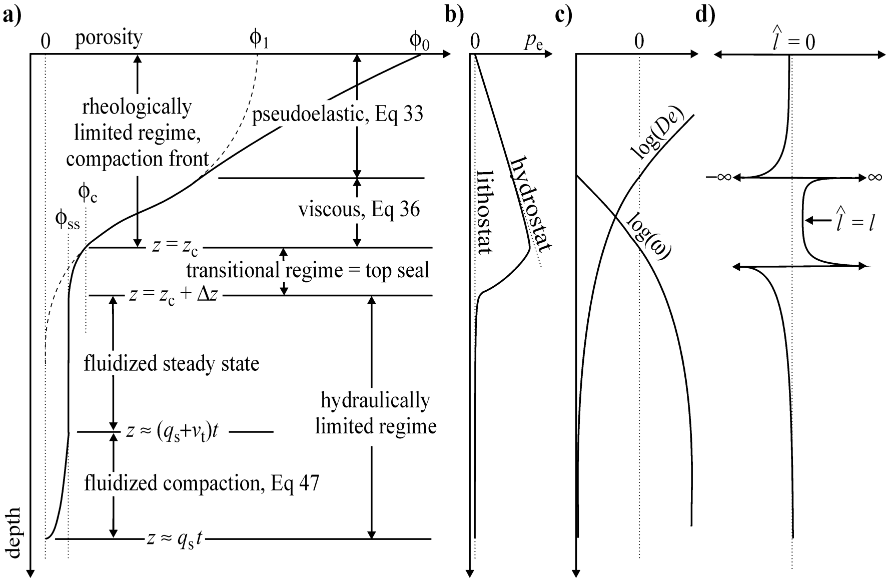

Fig. 2. Schematic sedimentary porosity (a) and effective pressure (b) depth profiles illustrating the quasi-steady-state compaction model. (c) Strong variation in ω and De [Eqs. (20), (21) and (30)] with depth and compaction is envisioned to divide the upper portion of the profile into four steady-state regimes. The fluid flux necessary to support the steady state must be derived by transient fluidized compaction at greater depth. Note that v_t is the velocity of the transition between the essentially non-compacting fluidized steady state and the compacting fluidized porosity measured relative to the sediment basement interface, i.e. $-v_t \le q_s$. (d) Schematic of the inverse model parameter $\hat{l}$ [Eq. (52)] obtained by fitting the gradient, curvature and porosity of a porosity profile with the analytical solution for viscous compaction [Eq. (36)] for $m \le 1$. Because the weakest, i.e. when $l \to \pm\infty$, curvature of the viscous compaction profile is generally stronger than the profiles characteristic of pseudoelastic and hydraulic compaction, and because finite positive values of l increase the viscous profile curvature, $\hat{l} > 0$ is diagnostic of viscous compaction.

porosity reduction, designated the compaction front (McKenzie, 1987). The compaction front is subtended by a transitional regime, characterized by $\omega \sim 1$, in which fluid overpressure grows rapidly as a consequence of consolidation. This regime is the model analogy of the top-seal of an overpressured sedimentary sequence. The transitional regime leads to conditions such that $\omega \gg 1$, whereupon fluid pressure is limited by the sediment load, i.e. the sediment is fluidized, and compaction is controlled entirely by drainage [Eq. (10) or (16)]. In this hydraulically limited regime, lithostatic pressures may not be realized if fracturing occurs at sublithostatic fluid pressure. However, if the yield condition that limits the proximity of the fluid pressure to the lithostat is a linear function of depth, as appears to be true in natural sedimentary environments (Mann and MacKenzie, 1990), our arguments remain applicable with fluid pressure gradient limited by an appropriately reduced mean stress gradient [Eqs. (9) and (10)].

Our treatment differs from earlier models of entirely pseudoelastic (Audet and Fowler, 1992; Wangen, 1992; Fowler and Yang, 1998) and entirely viscous (Sumita et al. 1996; Fowler and Yang, 1999) compaction in that we presume that the exponential dependence of the Deborah number [Eq. (30)] on depth leads to a transition from near-surface pseudoelastic compaction to viscous compaction. Such a transition is only of consequence if it occurs within the rheologically dominated regime, which is therefore the case we consider (Fig. 2d). Supposing the existence of a steady-state compaction regime at near-surface conditions requires that the steady-state domain must connect to a transient domain that produces exactly the fluid flux necessary to maintain the steady state. Such a connection is non-trivial because steady-state solutions of the viscous and viscoelastic compaction equations for arbitrary boundary conditions have a periodic antithetic variation of effective pressure and gradient (Sumita et al., 1996; Connolly and Podladchikov, 1998), a periodicity that is unlikely to be mimicked by any transient process. A near-surface steady state is thus only possible if the viscous regime approaches the non-periodic solitary steady state, in which both effective pressure and its gradient vanish at depth. As these conditions characterize the hydraulically limited regime, we seek a steady-state solution that extends into the hydraulically limited compaction regime as a means of quantifying the steady sedimentary compaction process. Our quasi-steady-state model thus consists of pseudoelastic ($\omega \ll 1$, $De \gg 1$), viscous ($\omega \ll 1$, $De \ll 1$), transitional ($\omega \sim 1$, $De \ll 1$), and fluidized ($\omega \gg 1$, $De \ll 1$) steady-state domains, succeeded by a domain of transient fluidized compaction. We follow the approach of Sumita et al. (1996), in that we approximate the fluidized steady-state domain as non-compacting. Because our interest is in the instability of the fluidized steady state, we do not attempt to characterize the viscoelastic transition ($\omega \ll 1$, $De \sim 1$) that occurs within the rheologically limited domain over a depth interval $\sim l$ [Eq. (30)].

3.1. Rheologically limited compaction

During rheologically limited compaction the effective pressure is $\Delta\rho g z$ and, using Eqs. (23) and (26) to describe the bulk viscosity in Eq. (17), the variation in porosity with depth is

$$\frac{\partial \phi}{\partial z} = -(1-\phi)\phi\left(\frac{(1-\phi)\phi^{m-1} z\, \mathrm{e}^{z/l}}{\lambda_{\mathrm{c}}^2} + \beta \Delta\rho g\right) \quad (31)$$

with

$$\lambda_{\mathrm{c}} = \sqrt{\frac{q_{\mathrm{s}} \eta_{\mathrm{r}}\, \mathrm{e}^{z_{\mathrm{r}}/l}}{\Delta\rho g}}. \quad (32)$$

The dependence of λ_{c} on l is artificial due to the specification of the reference viscosity, η_{r}, at finite depth, z_{r}. Thus, Eq. (31) can be made, i.e. if z_{r} is chosen as zero, to separate the temperature dependence of the compaction process from the remaining physical parameters of sedimentation (λ_{c} and ϕ_0). Although there is no general solution for the viscoelastic steady state [Eq. (31)], analytical solutions exist for the viscous and pseudoelastic limits. We explore these solutions as a means of constraining the rheological parameters of compaction.

3.1.1. Pseudoelastic compaction

The steady-state compaction profile during pseudoelastic compaction is given by the solution of Eq. (31) in the pseudoelastic limit ($\lambda_c \to \infty$)

$$\phi = \frac{\phi_0}{\phi_0 + (1-\phi_0)\,e^{\beta\Delta\rho g z}}. \tag{33}$$

This solution, which gives the quantity $(1/\phi - 1)$ as an exponential function of depth that is independent of sedimentation rate, is functionally similar to the simple exponential dependence originally proposed by Athy (1930) to describe near-surface sediment porosity

$$\phi = \frac{\phi_0}{e^{\beta\Delta\rho g z}}, \tag{34}$$

a solution obtained for Eq. (31) if the $1-\phi$ term is approximated as unity. Thus, both the exact and Athy solutions are capable of reproducing near-surface profiles if β is regarded as a free parameter; and the Athy solution approaches the exact solution as the initial sediment porosity becomes small. In detail, the complete solution has a weaker curvature that nears that of the Athy distribution with increasing depth or decreasing initial sediment porosity (Fig. 3a). The exact solution therefore explains overcompaction relative to the Athy distribution as commonly observed in the deeper sections of natural porosity profiles (Biot and Ode, 1965) and demonstrated by the profiles developed in intercalated shales and sandstones of the Pannonian Basin (Fig. 4, Szalay 1982, cited in Dovenyi and Horvath, 1988). This explanation has the virtue of simplicity in that it does not resort to the complexities, such as irregular variation in tectonic stress with depth, often invoked in basin modeling.

The coefficient of pore compressibility derived by regressing data from the upper 1200 m of the Pannonian porosity profiles is ($\pm\hat{s}$) $8.4 \pm 1.4 \times 10^{-8}$ and $4.0 \pm 0.5 \times 10^{-8}$ Pa^{-1} for the shales and sandstones, respectively. Neglect of true poroelastic effects in Eq. (9) is therefore justified given that typical elastic coefficients are an order of magnitude lower than these values (Palciauskas and Domenico, 1989). The compressibility of water is somewhat larger $\sim 10^{-8}$ Pa^{-1} at the conditions of interest, but the assumption of fluid incompressibility appears reasonable. Although the deviations from the pseudoelastic trend for the Pannonian

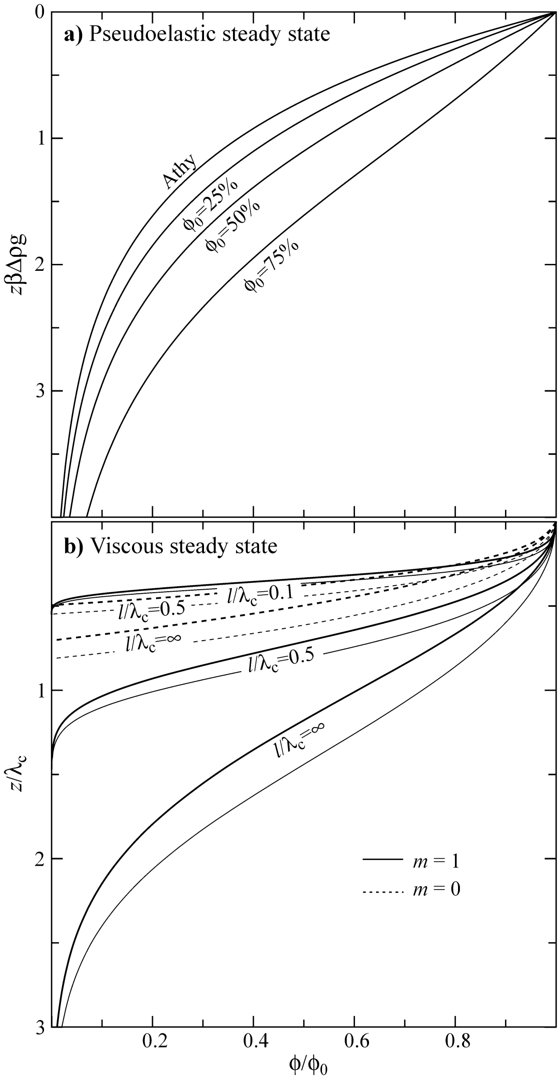

Fig. 3. Relative porosity as a function of dimensionless depth for pseudoelastic (a) and viscous (b) rheologically limited compaction. In the pseudoelastic limit, the exact solution [Eq. (33)] to the compaction equation approaches the Athy solution [Eq. (34)] as the initial sediment porosity becomes small. Heavy curves distinguish the exact viscous steady solution of Eq. (31) from the approximate solutions [Eqs. (35) and (36)] shown by thin curves for different values of l/λ_c and the limiting cases $m=0$ and $m=1$. In contrast to the pseudoelastic solution, the viscous solution is dependent on the sedimentation rate, as reflected in the parameter λ_c. With the exception of the approximate solution given by Eq. (35), the viscous steady state is dependent on the value of ϕ_1, which was taken to be 25% and identical to ϕ_0. The viscous profiles are bounded by the constant viscosity solution ($l \to \infty$, Eq. (37)], a reasonable approximation for $l/\lambda_c > 1$, which implies that thermal activation of viscous compaction is insignificant under such conditions.

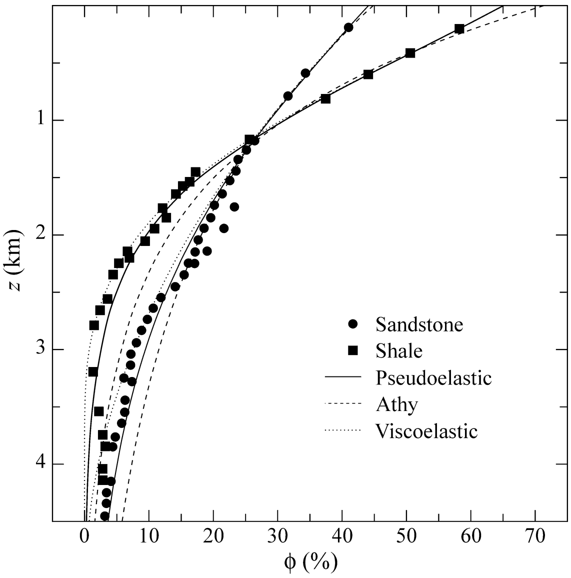

Fig. 4. Porosity trends of intercalated shale and sandstone lithologies of the Pannonian Basin as synthesized from borehole measurements in deep wells (Szalay, 1982 cited in Dovenyi and Horvath, 1988). Square and circular symbols represent averages over 100 m depth intervals. Dashed and solid curves show the Athy [Eq. (34)] and pseudoelastic [Eq. (33)] solutions regressed to shallow (<1260 m) bore-hole data. In both cases, the exact solution results in a significant improvement of the regression. The relative quality of the Athy solution is better for the sandstones, a behavior consistent with the result that the Athy solution is exact as $1-\phi\rightarrow1$ (Fig. 3). The exact solution explains overcompaction relative to the Athy profile as commonly observed in sedimentary sequences (Biot and Ode, 1965). The irregular variation in porosity at depth in the Pannonian Basin is due to hydrocarbon generation and devolatilization (Szalay, 1988; Clayton et al., 1990), mechanisms that are unlikely to cause overcompaction. Dotted curves show the viscoelastic solution of Eq. (31) with parameters discussed later in the text.

Basin profiles are subtle, we show subsequently that they are consistent with the existence of a viscous compaction mechanism.

3.1.2. Viscous compaction

With increasing depth, elevation of the effective pressure in combination with reduced sediment viscosity, increases the efficiency of the viscous compaction exponentially (Fig. 1b) so that the porosity profile must evolve toward a viscous steady state. To simplify the analytical solution for the viscous limit ($\beta\rightarrow0$), we approximate $1-\phi$ by unity. With this simplification, the general solution of Eq. (31) is

$$\phi=\left(\frac{1}{\phi_1^{m-1}}-(m-1)\frac{l(l-z)\,e^{z/l}-l^2}{\lambda_c^2}\right)^{-1/(m-1)} \tag{35}$$

and for the linear viscous case

$$\phi=\phi_1\exp\left(\frac{l(l-z)\,e^{z/l}-l^2}{\lambda_c^2}\right) \tag{36}$$

where ϕ_1 is the porosity at $z=0$, which is identical to ϕ_0 if the viscous domain extends to the surface. Comparison of these solutions with the exact solutions (Fig. 3b) suggests that for porosities similar to those at which viscous compaction commonly becomes evident during burial (~25%, Lundegard, 1992), the $1-\phi$ term in Eq. (31) is of minor consequence in view of the strong dependence of the steady state on the ratio l/λ_c. The dependence of the viscous steady state on l/λ_c indicates that the thermal activation is an essential feature of the compaction process when $l/\lambda_c<1$. The significance of λ_c is apparent in the limit that temperature dependence vanishes ($l\rightarrow\pm\infty$), in which case, a Taylor expansion of Eq. (36) simplifies to the Gaussian function similar to the solutions obtained in previous studies (Sumita et al., 1996; Connolly and Podladchikov, 1998; Fowler and Yang, 1999)

$$\phi=\phi_1\exp\left(-\frac{1}{2}\frac{z^2}{\lambda_c^2}\right) \tag{37}$$

such that the porosity falls to 1% of its initial value ϕ_1 at $z=3\lambda_c$. For finite positive l, and $m\leq1$, Eqs. (35) and (36) define porosity–depth profiles that have a stronger variation in porosity with depth than, and are bounded by, the corresponding Gaussian profile (Fig. 3b). Thus, λ_c defines the upper limit on the length scale over which underpressured porosity can be maintained during steady sedimentation. For example, if porosity is reduced by 87% of its initial value at depth z where the compaction process is arrested by the development of fluid overpressure, then λ_c $z/2$. This logic is independent of whether other mechanisms compete with viscous compaction, since the existence of these mechanisms merely requires that λ_c is greater than would be inferred for viscous compaction alone. Because λ_c is dependent on q_s (Figs. 4 and 5b), viscous compaction profiles are influenced by the sedimentation rate, in contrast to the pseudoelastic case.

In the context of sedimentary compaction, the pure viscous steady state described by Eqs. (35) and (36) must apply at depth when $De \to 0$. However, because pseudoelastic compaction affects the near-surface porosity, the value of ϕ_1 from the viscous steady state must be less than the true surface porosity. Consequently ϕ_1 becomes a fitting parameter that approximates the porosity at which viscous compaction becomes significant.

The maximum depth z_c of the viscous rheologically limited regime, from Eqs. (35) and (36), is given by the transcendental functions

$$(z_c - l)e^{z_c/l} = \frac{\lambda_c^2}{l}\left(\phi_c^{1-m} - \phi_1^{1-m}\right) - l \quad m \neq 1 \qquad (38)$$

$$(z_c - l)e^{z_c/l} = \frac{\lambda_c^2}{l}\ln\left(\phi_1/\phi_c\right) - l \quad m = 1 \qquad (39)$$

that can be expressed analytically in terms of the Lambert function and where ϕ_c is the porosity at the base of the rheologically limited regime. These equations give a weak dependence of z_c for $\phi_c \ll \phi_1$, a result that suggests that porosity–depth profiles formed by viscous compaction are dictated primarily by l and λ_c. Since λ_c defines the maximum extent of the compaction front and is a strong function of η_r and q_s (Fig. 5a), top seal formation at 2–4 km depth implies that values of l relevant to viscous compaction must be such that λ_c has little influence on the depth of the compaction front. Eq. (38) gives the ranges of λ_c consistent with these arguments as 1500–5000 and 5000–50 000 m for $l = 1500$ and 500 m, respectively (Fig. 6). The range of λ_c supported for $l = 1500$ seems narrow in view of natural variability, suggesting this value as an upper bound for viscous e-fold lengths characteristic of sedimentary environments. The upper limits on λ_c increase roughly threefold as $m \to 0$ (Fig. 6), an effect that does not substantially alter this conclusion. At 2–4 km depth, l is strongly dependent on the activation energy of the compaction process, with a relatively weak dependence on the geothermal gradient (Fig. 1a), a behavior also consistent with top seal formation over a narrow depth range. As observed effective pressure gradients are rarely $< \Delta\rho g/4$ (Mann and MacKenzie, 1990), η_r and v_s are the primary physical variables in λ_c. If time-averaged sedimentation rates are 10–1000 m/My, the range

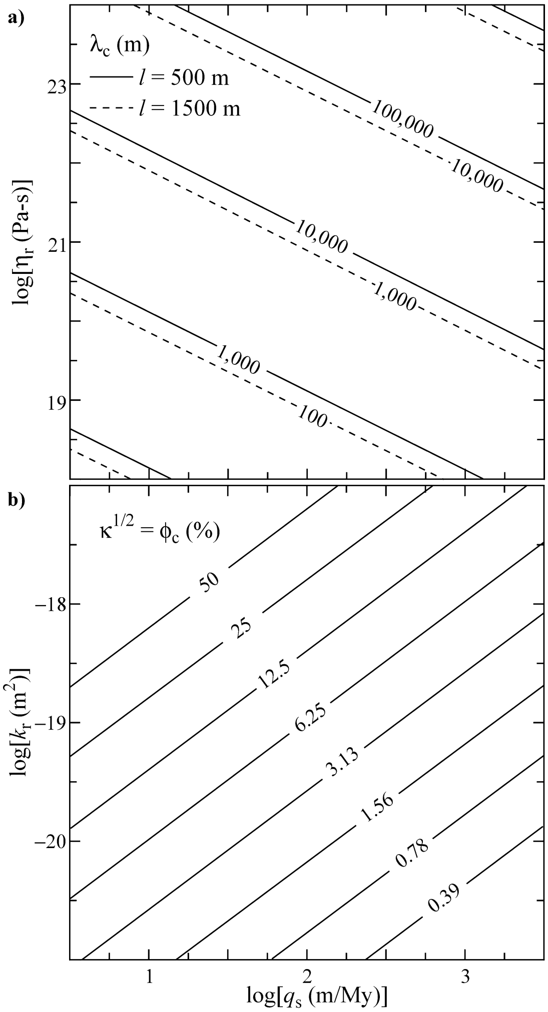

Fig. 5. (a) The rheological parameter λ_c [Eq. (32)] as a function of sedimentation rate and reference shear viscosity; parameters as in Table 1. (b) The hydraulic parameter κ [Eq. (41)] as a function of sedimentation rate and reference permeability. In the quasi-steady-state model, κ is the square root of the porosity at the depth of top-seal formation ϕ_c, and λ_c is the compaction length scale in the limit of a constant viscosity matrix.

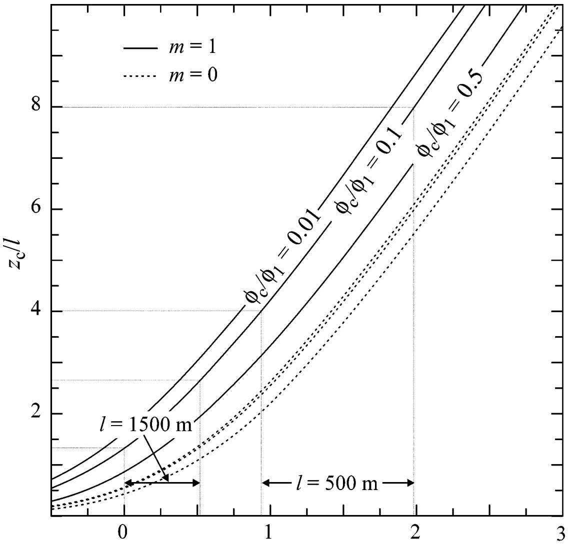

Fig. 6. Depth of top-seal formation (z_c, Eqs. (38) and (39)] during steady sedimentation as a function of ϕ_c, ϕ_1, m, l, and λ_c. For $m=1$, z_c is dependent on ϕ_c/ϕ_1 but independent of the individual porosities. In this case, provided viscous compaction causes a significant reduction in porosity, i.e. $\phi_c/\phi_1<0.5$, z_c is primarily a function of l and λ_c. In the general case, illustrated here by the extreme choice, $m=0$, z_c depends on both ϕ_c/ϕ_1 and ϕ_1, which is taken as 25%. To attain a given value of z_c with $m=0$, λ_c/l increases by half an order of magnitude compared to the linear viscous case, implying that for a given l and z_c, $v_s\eta_r$ must increase by an order of magnitude. Thin dashed lines indicate the range of λ_c supported by $l=500$ and 1500 m, with $m=1$ and $\phi_c/\phi_1=0.1$, for top-seal formation at depths of 2–4 km. For $l=1500$ m, $\lambda_c=1500$–5000 m, whereas for $l=500$ m, $\lambda_c=5000$–50 000 m. A narrow range of top-seal depth in nature, despite the likely variability of λ_c, therefore requires values of $l<z_c$.

for η_r from this analysis is 10^{19}–10^{23} Pa-s with $m=1$, and an order of magnitude higher for $m=0$.

3.2. Transitional compaction regime

The transitional steady-state compaction regime (Fig. 2a) is bounded by the conditions under which the effective pressure gradient vanishes, so that the porosities ϕ_c and ϕ_{ss} are the roots of Eq. (16) at its upper and lower limits. As ϕ_c is presumed large compared to ϕ_{ss}, the approximate form of Eq. (16) with Eq. (21) gives the transitional porosity at which overpressure begins to deviate strongly from that of normal fluid pressures as

$$\phi_c \approx \sqrt[n-1]{\kappa} \tag{40}$$

where κ (Fig. 5b) represents the constant component of the approximate form of ω, i.e.

$$\kappa = \frac{\omega}{\phi^n} \approx \frac{\phi_r^n \mu q_s}{k_r \Delta\rho g}. \tag{41}$$

Given the implausibility of values of $m<1$ at small porosity, we assume hereafter that $m=1$ at $z<z_c$. To determine the asymptotic limit of the steady-state porosity ϕ_{ss}, $(\partial\phi/\partial z)$ in Eq. (17) is expanded as $(\partial\phi/\partial p_e)(\partial p_e/\partial z)$, and Eq. (16) is used to define $(\partial p_e/\partial z)$ in terms of the model parameters. The resulting expression for $(\partial\phi/\partial p_e)$ then is integrated from $p_e=z_c\Delta\rho g$ to $p_e=0$ to obtain the change in porosity across the transitional regime. For $1-\phi\sim 1$ and $\phi_c/\phi_{ss}>2$, the result of exact integration is well approximated by

$$\phi_{ss} \approx \left(\frac{2\kappa\lambda_c^2}{z_c^2\, e^{z_c/l} n(n-1)}\right)^{1/(n-1)}. \tag{42}$$

We show below that conditions such that $\phi_{ss}\sim\phi_c$ are not of interest because the steady state is then inherently unstable. Within the transitional regime, the effective pressure gradient is a strong function of depth, but to characterize the conditions, we introduce the proxy function, $k(\partial p_e/\partial z)$, which must reach a maximum within the regime. The characteristic porosity obtained by equating the second derivative of the proxy to zero is $\sqrt[n-1]{\kappa/n}$. Substituting this porosity into Eq. (16), the characteristic effective pressure gradient $(\partial p_e/\partial z)^*$ is $(1-n)\Delta\rho g$. The porosity within transitional regime is then approximated by a second-order Taylor expansion of the solution to Eq. (17) about $z=z_c$, for the characteristic effective pressure gradient and the boundary conditions $\phi=\phi_c$ and $p_e=\Delta\rho g z_c$ at z_c, as

$$\phi \approx \phi_c \times \exp\left(l\,\frac{[(n-1)(z-1)+nz_c]\,e^{z/l}+[(n-1)l+z_c]\,e^{z_c/l}}{\lambda_c^2}\right). \tag{43}$$

Because $(\partial p_e/\partial z)^*$ is ad hoc, Eq. (43) may reach a minimum at $\phi > \phi_{ss}$ (Fig. 2a), in which case, the profile in the transitional regime must be extrapolated to the steady-state porosity by other means.

3.3. Transient compaction and stability of the steady state

Maintenance of the steady-state porosity ϕ_{ss} requires a constant fluid flux that, in the absence of an external source, must be derived by transient fluidized compaction at a greater depth. For transient fluidized compaction, Eq. (10) with Eq. (21), can be rearranged to

$$\frac{1}{1-\phi}\frac{\partial \phi}{\partial t} = -\frac{\partial \phi}{\partial z}\left(\frac{n}{\kappa}\phi^{n-1} + v_s\right). \tag{44}$$

Since the perturbation caused by fluidized compaction on the sediment velocity is smaller than for steady-state compaction [Eq. (8)], we approximate $1-\phi$ by unity and assume that the fluidized region grows upward from the sediment–basement interface at which the porosity is zero. The solution to Eq. (44) obtained by the method of characteristics is then

$$\phi = \left(-\frac{\kappa v_t}{n}\right)^{1/(n-1)}\left(1+\frac{z'}{v_t t}\right)^{1/(n-1)} \quad 0 \leq -\frac{z'}{v_t t} \leq 1 \tag{45}$$

where v_c is the velocity of the transition to fluidized compaction relative to the sediment basement, $z' = z - z_c - (v_s + v_t)t$, and $t = 0$ when the sediment-basement interface first reaches $z = z_c$ (Fig. 2a). Since the porosity at $z' = 0$ must be ϕ_{ss} if the compaction equations have a steady-state solution, Eq. (45) requires

$$\phi_{ss} = \left(-\frac{\kappa v_t}{n}\right)^{1/(n-1)}. \tag{46}$$

Equating Eqs. (42) and (46) to solve for v_c, with $v_s \approx q_s$, gives

$$\frac{v_t}{q_s} = \frac{-2\lambda_c^2}{z_c^2\, e^{z_c/l} n(n-1)}. \tag{47}$$

If $v_t/v_s < -1$, then the steady state extends to a growing region of non-compacting fluidized porosity (Fig. 2a) that is truncated by the region of fluidized compaction. The alternative to this condition implies that the sedimentary column grows less rapidly than the region of transient compaction, and therefore that steady-state compaction is not possible. For likely parameter ranges (Fig. 6), $\lambda_c^2/(z_c e^{z_c/l}) < z_c$; thus, we conclude that the steady state is generally the appropriate model for the compaction process during uniform sedimentation. This conclusion implies that the formation of a top seal is a natural consequence of sedimentary compaction, but it does not preclude the development of transient instabilities beneath the top seal in response to perturbations of the sedimentary process, a possibility that we treat subsequently. The width, Δz, of the transitional regime estimated by equating a second-order Taylor expansion of Eq. (43) to Eq. (46) is

$$\Delta z \approx \frac{\lambda_c^2}{z_c\, e^{z_c/l}}, \tag{48}$$

which, for parameters as above, gives top seal thicknesses generally less than, or comparable to, the viscous e-fold length. From Eqs. (45) and (3), the fluid velocity below z_c is

$$v_f = \frac{z'}{t'n} - v_t\left(1 - \frac{1}{n}\right) \tag{49}$$

giving a minimum, downward, fluid velocity of $-2/3v_t$ [i.e. $-v_t(1-1/n)$ for $n = 3$] that increases with time and depth. This result is consistent with the expectation that once fluidization occurs, fluid-filled porosity is advected downward by burial with little compaction, a necessary condition for the steady state.

3.4. Numerical verification and transient calculations

To assess the applicability of the quasi-steady-state model, we solve the transient compaction equations numerically. Since the maximum transient deviations from the steady-state model must develop in the transitional regime, for numerical simplicity, we consider viscous compaction with an initial porosity of 25%. Under these conditions, the approximations that $1-\phi \approx 1$ and that the sediment velocity is constant are justified, as demonstrated earlier (Fig. 3b), and Eqs. (9) and

(10) simplify to

$$\frac{\partial\phi}{\partial t'}=-\frac{\phi^m}{\lambda_c}p'-\frac{\partial\phi}{\partial z'} \tag{50}$$

$$\frac{\partial\phi}{\partial t'}=\frac{1}{\kappa}\frac{\partial}{\partial z'}\left(\phi^n\left(1-\frac{1}{\lambda_c}\frac{\partial p'}{\partial z'}\right)\right)-\frac{\partial\phi}{\partial z'} \tag{51}$$

where primes indicate the non-dimensional variables as defined for Eqs. (18)–(20), with $L=\lambda_c$, and dimensionless time, t/t^*, is defined relative to the characteristic time, $t^*=L/q_s$; and λ_c and κ are as in Eqs. (32) and (41). The non-dimensional form of the transient compaction equations show that if η_r is increased by an order of magnitude, and k_r and q_s are decreased by an order of magnitude, the transient evolution is unaffected in non-dimensional time, but that the dimensional time scale increases by an order of magnitude.

For parameters near the extremes pertinent to natural environments, numerical solutions to Eqs. (50) and (51) (Fig. 7) show no significant time dependence of the porosity profile above the fluidized compaction regime. The proximity of the profiles to the analytical steady-state model confirms the validity and accuracy of the analytical approximation as a tool for the prediction of the depth of top-seal formation and the amount of fluid likely to be trapped beneath the top-seal. In detail, fluid overpressure within the compaction front hinders compaction in the rheological limited regime, resulting in profiles that are slightly undercompacted relative to the analytical steady state. Factors that increase the curvature of the compaction front, i.e. lower m or l, cause a more rapid dissipation of this overpressure and a closer approach to the conditions assumed for the analytical model [Eqs. (35 or 36)].

If sedimentation is interrupted, the upper portion of the porosity profile remains pinned by the surface boundary, where the effective pressure vanishes, but the lower portion of the profile is propagated upward with velocities that decay exponentially upward due to thermal activation (Fig. 1a). It follows that although the porosity distribution within the compaction front may be sensitive to sedimentation rate, after the cessation of sedimentation, the compaction front must rapidly evolve toward a common state that is dictated largely by l and only weakly dependent on the initial sedimentation rate. Moreover, because the initial difference between the velocity of the compaction front and subjacent fluid is $\ll -2/3q_s$ [Eq. (49)], this evolution is independent of sediment permeability. This state is not truly stationary because the base of the compaction front has a finite velocity [approximated by Eq. (29)], but it is none the less described well by Eqs. (35 or 36) if the sediment velocity is replaced by an estimate of the velocity of the front (Fig. 8).

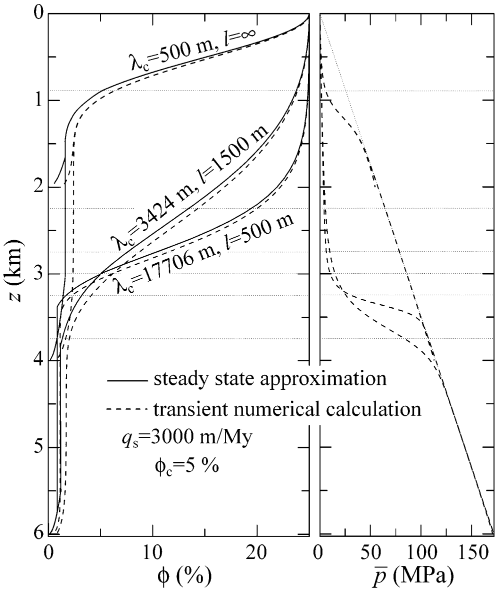

Fig. 7. Comparison of the analytical quasi-steady-state model (solid curves) with numerical models (dashed curves) of the transient evolution of porosity (a) and overpressure (b) during sedimentation. The results have been made dimensional taking $q_s=3000$ m/My for $\phi_c=\kappa^{1/2}=5\%$ [$k_r=1.2\times10^{-18}$ m^2, Eq. (46)] with remaining parameters as in Table 1. Numerical results for constant viscosity ($l=\infty$, $\lambda_c=500$ m, $\eta_r=4.5\times10^{19}$ Pa-s) demonstrate the general result that within the compaction front ($\phi>\phi_{ss}$), transient effects are insignificant. For the finite viscous e-fold length calculations, λ_c has been chosen to give the transitional compaction regime, i.e. top seal formation, at $z_c=3000$ m. In all models, the width of transitional regime is predicted well by Eq. (48). The discrepancy between the analytical and numerical steady state within the compaction front is due to overpressure that is not accounted for in the rheologically limited compaction regime. The maximum overpressure increases as ϕ_c/ϕ_1 and is dissipated more rapidly in models with low m or l.

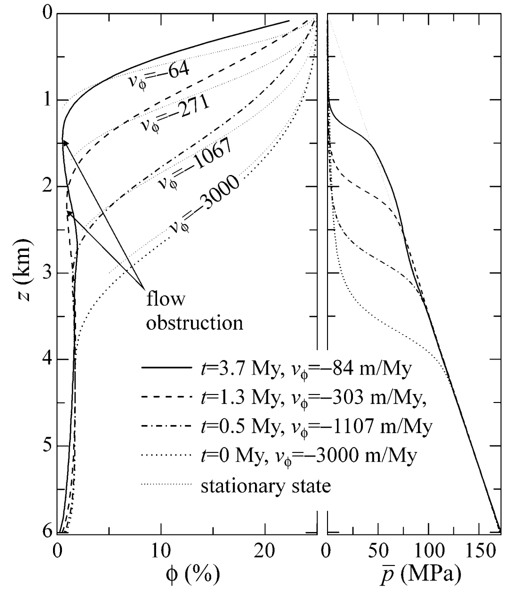

Fig. 8. Numerically computed porosity and fluid overpressure evolution and incipient flow instability following the cessation of steady sedimentation at $t=0$. Calculations were made dimensional by choosing $q_s=3000$ m/My at $t<0$, $k_r=1.2\times10^{-18}$ m^2, $\eta_r=2.8\times10^{20}$ Pa-s with $l=1500$ m, $\lambda_c=3424$ m and $\sqrt{\kappa}=5\%$. The porosity phase velocity (at $\phi=6.25\%$) compares well with the phase velocity obtained by computing λ_c for the stationary state [thin dotted curves, Eq. (36)] from the depth at which $\phi=6.25\%$ in the transient profile; phase velocities estimated from Eq. (29) are about three times those obtained numerically. The compaction front propagates upward with an initial velocity $\approx -q_s$, whereas the maximum fluid velocity beneath the front is $\ll -2/3q_s$ [Eq. (49)]. Consequently, the porosity collapses as the front propagates, creating an obstruction to fluid flow from beneath the front that causes supralithostatic fluid pressure and secondary porosity generation. A high sedimentation rate is not a requirement for instability, e.g. if q_s and k_r are decreased by two orders of magnitude and η_r increased by two orders of magnitude, the evolution is unchanged except that the time scale increases in direct proportion to η_r.

3.5. Application to the Pannonian Basin

Direct application of the quasi-steady-state compaction model is not feasible because of the uncertainty in the rheological parameters of the model. As an alternative, we employ an inverse model to constrain the parameters and porosity dependence of natural compaction processes from sedimentary porosity profiles as illustrated here by application to the Pannonian Basin, which contains 6–7 km of sediment accumulated over the last 17.5 My (Royden and Horvath, 1988). The basin stratigraphy can be simplified to a mixture of shales and sandstones with different porosity trends (Fig. 9, Szalay 1982, cited in Dovenyi and Horvath, 1988).

The shape of porosity profiles formed by viscous compaction is limited by a Gaussian function ($m\leq1$, Eqs. (35) and (36)], a shape consistent with commonly observed deviations from the Athy porosity–depth distribution in the deeper sections of natural profiles (e.g. Biot and Ode, 1965; Schneider et al., 1996). At $z<\lambda_c$, the curvature of the Gaussian profile [Eq. (37)] is stronger than both the exponential pseudoelastic distribution, and the distribution attainable during hydraulically limited compaction [Eq. (43)]. Thermal activation in a normal geothermal gradient results in positive values of l, which gives rise to a porosity depth dependence that is even stronger than the limiting Gaussian profile (Fig. 3b). It follows that to fit the viscous steady-state solution [Eq. (36)] to a profile characteristic of hydraulic or pseudoelastic compaction, the fitted value of the viscous e-fold length, $\hat{l}$, must be negative and approach negative infinity as the curvature becomes increasingly influenced by viscous compaction (Fig. 2d). In contrast, if the equations are fit over a depth interval where viscous compaction is dominant, $\hat{l}=l$, but will deviate toward positive infinity if the influence of hydraulic or pseudoelastic compaction becomes significant. If an observed porosity trend is fit by an arbitrary function, then equating this function to Eq. (36) (i.e. $m=1$) and its derivatives gives a system of non-linear equations that can be solved for the fitting variables:

$$\hat{l}=\frac{z\phi\phi'}{z\phi\phi''-z\phi'^2-\phi\phi'} \tag{52}$$

$$\hat{\lambda}_c=\sqrt{-\frac{z\phi}{\phi'}\,e^{z/\hat{l}}} \tag{53}$$

$$\hat{\phi}_1=\phi\exp\left(\frac{\hat{l}^2+\hat{l}(z-\hat{l})\,e^{z/\hat{l}}}{\hat{\lambda}_c^2}\right), \tag{54}$$

where $\hat{l}$, $\hat{\lambda}_c$ and $\hat{\phi}_1$ become identical to the model parameters, l, λ_c, and ϕ_1, in the limit of pure viscous steady-state compaction, and ϕ' and ϕ'' are

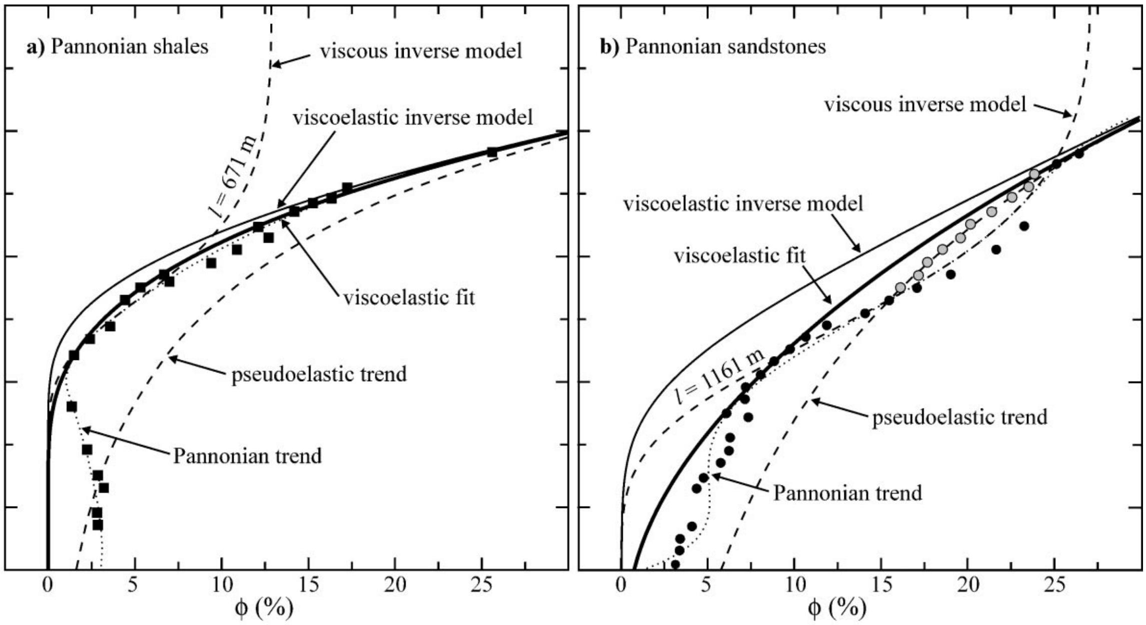

Fig. 9. Porosity trends in shales (a) and sandstones (b) of the Pannonian Basin (see Fig. 4 for complete data and description). Dashed curves show the near-surface pseudoelastic trend (Fig. 4). Dotted curves show the porosity trend (excluding sandstone data indicated by shaded circles, Fig. 10). Deviations from the pseudoelastic trend are attributed to viscous compaction. Dash-dotted curves show the viscous component of the compaction profile, as inferred from the inverse of the viscous steady-state solution (Fig. 10). The rheologically limited compaction model becomes invalid as the porosity approaches ϕ_c for the shales (short-dashed curve). The thin solid curve shows the viscoelastic solution of Eq. (31) obtained with ϕ_0 and $\beta\Delta\rho g$ from the pseudoelastic trend (Fig. 4) and λ_c and l from the inverse viscous solution. The heavy solid curve shows the viscoelastic solution (see also Fig. 4) obtained when λ_c is varied to fit the porosity at 2800 m depth. For both profiles, this procedure requires $\lambda_c = 10\,300$ m, corresponding to a two- to fivefold increase in the inferred value of η_r.

the first and second derivatives of the profile. Eqs. (52)–(54) ideally lead to a solution in which there is a broad local minimum at $\hat{l} = l$, defining a depth interval of viscous dominated compaction; bounded by maxima representing the transitions to the pseudoelastic and hydraulic compaction regimes (Fig. 2d).

As discussed earlier (Fig. 4), the near-surface Pannonian porosity trends are consistent with pseudoelastic compaction, but the trends deviate markedly from this behavior at depth. In the case of the sandstones, the scatter of the data at 1300–2200 m depth suggests two distinct populations: one that follows the near-surface pseudoelastic trend (open circles, Fig. 9), and another that appears to be continuous with the overcompacted trend at depth. Excluding the former data, each profile was fit with an arbitrary polynomial function (Fig. 10), which was then used to express the porosity and its derivatives with respect to depth in Eqs. (52)–(54). The results are satisfying in that the depth of the transition to hydraulically limited compaction is virtually identical (2790 vs. 2822 m, Fig. 10a), as consistent with the expectation that the lithology with the lower effective permeability dictates the development of overpressure in both lithologies. In contrast, the transition from pseudoelastic to viscous compaction is likely to be lithologically controlled, with pseudoelastic compaction operating at greater depths in clay-rich sediment (e.g. Ashby, 1988), as also suggested by the Pannonian profiles. Although these profiles are nearly a realization of the ideal scenario, the local minima in $\hat{l}$ are not broad (Fig. 10a). In the context of the model, this indicates that hydraulic and pseudoelastic compaction are significant in the viscous regime, with the result that the minima in $\hat{l}$ give upper limits on l. Because $\hat{l}$ has almost

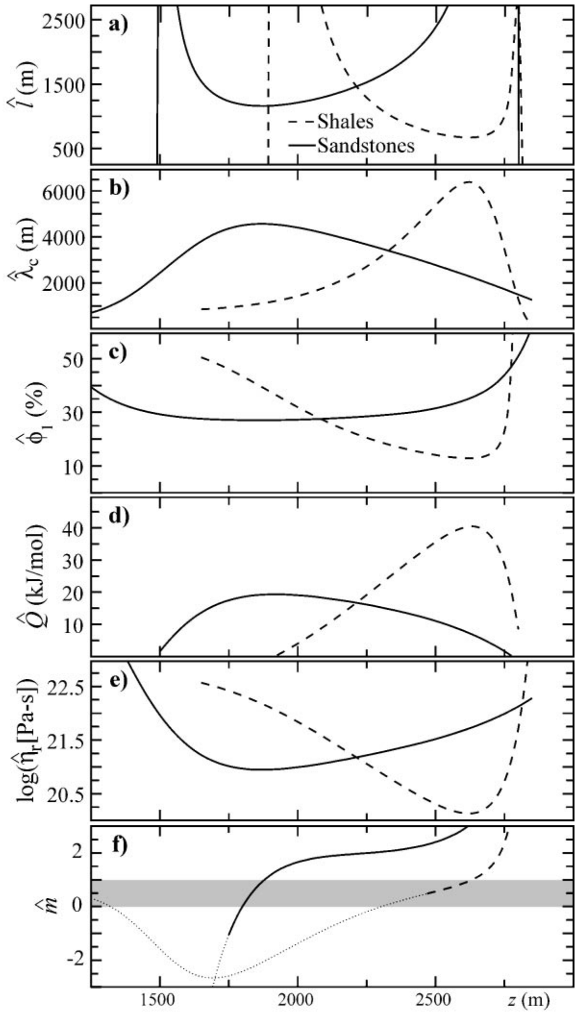

Fig. 10. Inverse solution to the viscous steady-state profile for the sandstone and shale porosity trends of the Pannonian basin (Fig. 9). (a–c) Inverse model parameters assuming $m=1$ [Eqs. (52)–(54)]; under this assumption, $\hat{l}>0$ is diagnostic of viscous compaction, and the minimum value of $\hat{l}$ must approach l (Fig. 2d). Estimators for Q (d) and η_r (e) from the inverse solution, assuming a geothermal gradient of 50 K/km and an average sedimentation rate of 350 m/My. (f) If the assumption $m=1$ is relaxed, $\hat{m}$ [Eq. (55)] estimates m. Values of $\hat{m}$ for which $\hat{l}<0$ [from Eq. (56)], indicated by thin dotted portions of the curves, are not physically meaningful. The exponent, m, is expected to have values between zero and unity (shaded region). For the solution, observed porosities (Fig. 9) were fit to $\phi=a+bz+cz^2+dz^3+ez^4+fz^5$ in the range $z=1000$–3500 m, giving ($\pm\hat{s}$): $\{a=0.62406\ \pm0.02,\ b=-1.4422\pm0.4\times10^{-3},\ c=-4.4919\pm0.4\times10^{-6},\ d=3.7647\pm0.2\times10^{-8},\ e=-1.1784\pm1.1\times10^{-13}, f=-1.3323\ \pm0.1\times10^{-17}\}$ and $\{a=0.80973\pm0.01,\ b=-1.2780\pm0.08\times10^{-3},\ c=1.1809\pm0.01\times10^{-6},\ d=-5.3875\pm0.005\times10^{-8},\ e=1.1309\pm0.1\times10^{-12},\ f=-8.8023\pm1.0\times10^{-18}\}$ for shales and sandstones, respectively.

perfectly sympathetic and antithetic relationships to $\hat{\phi}_1$ and $\hat{l}_c$, the analysis gives lower and upper bounds on ϕ_1 and λ_c. These bounds are $\{l<671$ m, $\lambda_c<6417$ m, and $\phi_1>12.8\%\}$ and $\{l<1161$ m, $\lambda_c<4572$ m, and $\phi_1>27.0\%\}$ for the shales and sandstones, respectively. For Pannonian geothermal gradient (~50 K/km, Dovenyi and Horvath, 1988), the bounds on l correspond to activation energies of 19.3 and 40.6 kJ/mol [Eq. (27), Fig. 10d]; the former value, for the sandstones, is essentially the value of 20 kJ/mol commonly quoted for pressure solution creep of quartz-rich rocks (e.g. Angevine and Turcotte, 1983; Rutter, 1983; Shimizu, 1995; Schneider et al., 1996). For the average sediment velocity at 2 km depth (~350 m/My) and normal fluid pressures, the limits on λ_c give $\eta_r>10^{20}$–10^{21} Pa-s [Eq. (39), Fig. 10e], in agreement with independent estimates of effective viscosity of near-surface sediments from models of salt diapirism (Poliakov et al., 1993b) and basin subsidence (Gratz, 1991).

The values of λ_c and l deduced from the inversion of the viscous steady state combined with the values of ϕ_0 and $\beta\Delta\rho g$ obtained by regression of the pseudoelastic model to the near-surface porosity (thin solid curves, Fig. 10) completely parameterize the rheologically limited viscoelastic steady state [Eq. (31)]. The profile obtained by solving Eq. (31) with the shale parameters is remarkably similar to the observed profile. That the same exercise for the sandstone parameters is less successful is not surprising in view of the inconsistencies in the sandstone data discussed previously. For both lithologies, the steady-state profiles are overcompacted relative to the data, a discrepancy consistent with the influence of pseudoelastic mechanisms and incipient overpressuring at the depths at which the viscous parameters were inferred. The porosity at the depth of incipient fluidization in both lithologies is fit with $\lambda_c=10\,300$ m (heavy solid curves, Fig. 9). If the remaining variables that comprise λ_c are held constant, then this value would correspond to a two- to fivefold increase in the value of η_r inferred by the inverse method.

The Pannonian shales are three orders of magnitude less permeable than the sandstones (Szalay, 1982, cited in Van Balen and Cloetingh, 1994) and therefore determine the effective permeability of the hydraulic regime (Qin and Ortoleva, 1994). The increase in the porosity of the shales at depths >3 km is due to secondary porosity generation thought to be caused by overpressures resulting from compaction, hydrocarbon maturation, and decarbonation reactions (Szalay, 1988; Clayton et al., 1990). The irregular porosity profile of the sandstones at depth is understandable as sandstone porosities would be dictated by the fluid flux supported by the shales. For the depth of the transition to hydraulically controlled compaction indicated by both Pannonian porosity profiles ($z_c=2800$ m, Fig. 10), Eqs. (38) and (40) give $\phi_c=\kappa^{1/2}=1.3\%$ with parameters from the viscous steady-state solution for the shales. This range compares to the minimum porosity (1.36% at $z=$ 3200 m) of the shale profile and the empirical trend, for which $\phi=1.3\%$ at 2800 m.

Numerical calculations using κ, λ_c and l deduced from the analytical solution show that the Pannonian basin overpressures are at least partially explicable as a consequence of the transition to hydraulically controlled compaction. If the calculations are made dimensional by taking $q_s=350$ m/My, and parameters as in Table 1, the reference permeability ($k_r=2\times10^{-19}$ m^2) required for the numerical calculation to match the minimum porosity compares with the permeability $k_r\sim10^{-19.5}$ m^2 from empirical functions fit to Pannonian sediment data (Van Balen and Cloetingh, 1994). The numerical calculations in which sediment viscosity was computed as an explicit function of temperature [Eq. (25)], show that the approximation that l does not vary with depth is justified (Fig. 11). Because the effective pressure gradient is large within the compaction front (Szalay, 1988), the value of λ_c deduced from

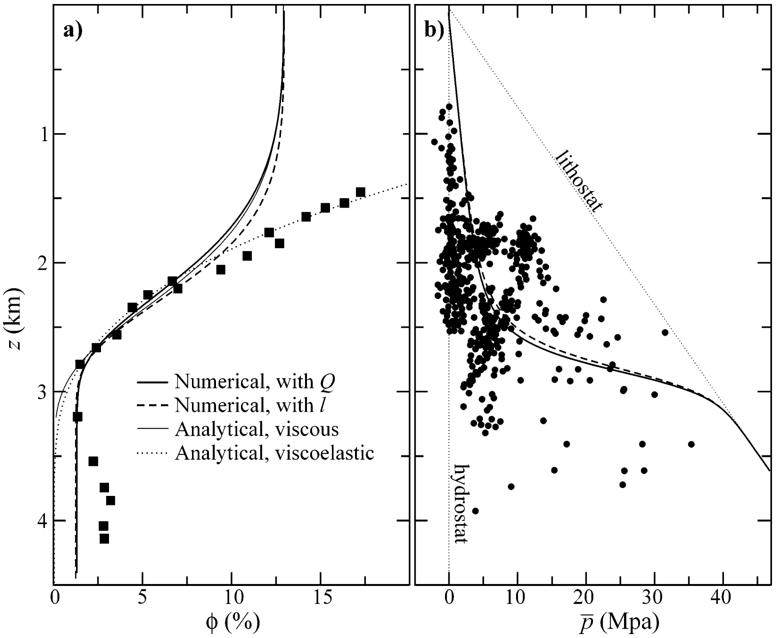

Fig. 11. Porosity (a) and pressure (b) profiles for Pannonian shales made dimensional with $q_s=350$ m/My and viscous model parameters inferred from the inverse model (Fig. 10) compared with Pannonian trends (porosities from Szalay, 1982 cited in Dovenyi and Horvath, 1988, overpressures from Clayton et al., 1990). The permeability used for the calculations, $k_r=2\times10^{-19}$ m^2, chosen to reproduce the observed porosity at 2820 m depth is an order of magnitude lower than estimated from the inverse model, but agrees well with shale permeability measurements ($k_r\sim10^{-19.5}$ m^2, Szalay, 1982 cited in Van Balen and Cloetingh, 1994). A comparison of numerical calculations made with a constant viscous e-fold length (671 m) with those made with constant activation energy ($Q=$ 40.5 kJ/mol, $\nabla T=0.05$ K/m), shows that the assumption of constant l has minor influence on the computational results.

the profiles is largely independent of the overpressure, as demonstrated by the similarity of the numerical and analytical solutions.

The general form of the viscous steady state [Eq. (35)] can, in principle, be used to deduce the porosity dependence of the bulk viscosity as well as the remaining parameters of viscous compaction. For the general form

$$\hat{m} = -\frac{\phi^2(\phi'''\phi' + \phi''^2 + \phi'^2 z^{-2})}{\phi'^2(\phi''\phi - \phi'^2)} \tag{55}$$

$$\hat{l} = \frac{z\phi\phi'}{z\phi\phi'' - \hat{m}z\phi'^2 - \phi\phi'} \tag{56}$$

$$\hat{\lambda}_c = \sqrt{-\frac{z\phi^{\hat{m}}}{\phi'}\,\mathrm{e}^{z/\hat{l}}} \tag{57}$$

$$\hat{\phi}_1 = \left(\frac{1}{\phi^{\hat{m}-1}} + \frac{(\hat{m}-1)\hat{l}((\hat{l}-z)\,\mathrm{e}^{z/\hat{l}} - \hat{l})}{\hat{\lambda}_c^2}\right)^{-1/(\hat{m}-1)}. \tag{58}$$

The values of $\hat{m}$ from the Pannonian porosity profiles (Fig. 10f) are of doubtful significance because of the error in assessing the third derivative of the profile, but the local extrema in $\hat{l}$, $\hat{\lambda}_c$ and $\hat{\phi}_1$ when $m = 1$ is assumed correspond to the depth at which $\hat{m} = 1$ when m is not constrained. The minimum value of $\hat{m}$ at which the remaining parameters have meaningful values from the shale profile is 0.5 at $z = 2466$ m $\{l < \infty$, $\lambda_c < 2376$ m, $\phi_1 > 23.4\%$, $Q > 0$, $\eta_r < 1.1 \times 10^{22}$ Pa-s$\}$, whereas for the sandstone profile, $\hat{m}$ spans the entire theoretical range, with $\hat{m} = 0$ at $z = 1799$ m $\{l < 2312$ m, $\lambda_c < 6740$ m, $\phi_1 > 27.5\%$, $Q > 9.5$ kJ/mol, $\eta_r < 3.1 \times 10^{21}$ Pa-s$\}$. Values of $m > 1$ weaken the depth dependence of the curvature of the steady-state profile. Therefore, large $\hat{m}$ values for the Pannonian profiles at depth are interpreted as an indication of hydraulically limited compaction.

4. Compaction-generated flow instabilities

Compaction gives rise to a quasi-steady-state porosity–depth profile in which two distinct compaction regimes are connected by a narrow transitional zone. The proximity of the upper, rheologically limited regime to a stationary state demonstrates that the upper portion of the profile responds rapidly to perturbations of the sedimentary process, i.e. on a time scale of $\sim l v_\phi$ (Fig. 1b). In contrast, beneath the compaction front, the porosity profile is essentially static in a reference frame that moves with the sediments. Consequently, if the sedimentation rate changes, the porosity at the base of the compaction front will evolve toward a new value that is largely independent of processes at greater depth. This porosity varies as q_s^{n-1} [Eq. (46)], and as the depth of this value of the porosity is proportional to the sedimentation rate through λ_c, a reduction in sedimentation rate creates a low-porosity obstruction to fluid flow from beneath the compaction front (Fig. 8). It is well established that a flow obstruction will cause nucleation of flow instabilities manifest as porosity waves (e.g. Barcilon and and Richter, 1986). In contrast, an increase in sedimentation rate does not generate flow instabilities because it causes the compaction front to develop higher porosities at a greater depth than the initial quasi-steady state.

4.1. Porosity waves in a viscous matrix

The numerical calculation depicted by the heavy solid curves in Fig. 12 provides a basis for understanding the evolution of porosity waves during a sedimentary hiatus (commencing at $t = 0$). Because the velocity of the compaction front grows exponentially with depth (Fig. 1a), the front forms a significant obstruction to fluid flow shortly after the cessation of sedimentation. The fluid pressure then increases beneath the obstruction, but because the obstruction has a finite permeability, the pressure diffuses into the obstruction creating a domain of negative effective pressure about the initial depth of the compaction front (i.e. supralithostatic pressures, at $t = 1.2$ My and $z = 2.5$–3.2 km, Fig. 12b). Within this domain, pore dilation increases the permeability, but the fluid flux within the dilated region must be less than in the deeper undeformed rocks. From Darcy's law, the fluid flux is proportional to the product of the overpressure gradient and the permeability, thus the fluid pressure gradient within the domain relaxes

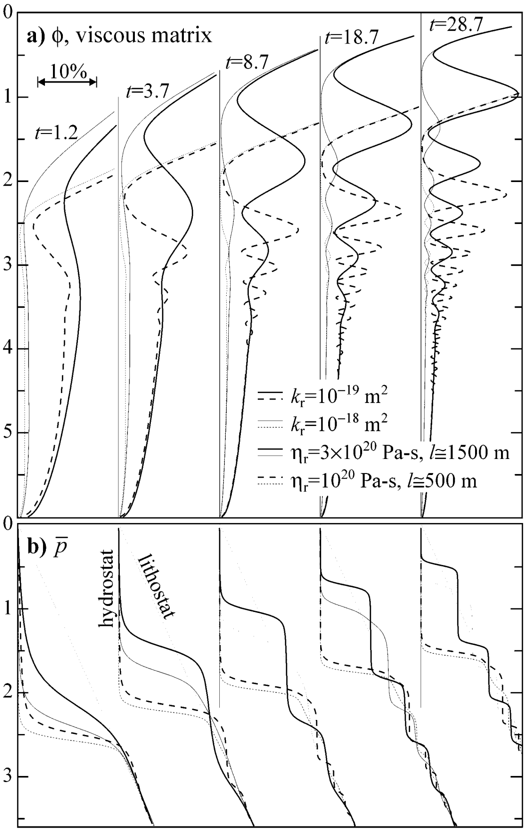

Fig. 12. Numerically calculated porosity (a) and overpressure (b) profiles for viscous sediment at approximately exponentially increasing time intervals after the cessation of steady sedimentation ($q_s=3000$ m/My, $\phi_1=25\%$). The calculations were made for constant Q (20 or 60 kJ/mol) with $\nabla T=50$ K/km, and the respective values of Q give l values to equal 500 and 1500 m at 3 km depth. For $\eta_r=2.28\times10^{12}$ Pa-s ($l=1500$ m) and $k_r=1.17\times10^{-18}$ m^2: $\lambda=4300$ m, $z_c=3$ km, $\phi_c=5\%$, $\tau_c=0.088$ My. For $\eta_r=10^{20}$ Pa-s ($l=500$ m) and $k_r=1.17\times10^{-18}$ m^2: $\lambda_c=17\,700$ m, $z_c=3$ km, $\phi_c=5\%$, $\tau_c=0.014$ My. Decreasing k_r raises ϕ_c, thereby increasing z_c and τ_c [Eq. (28)]. The local viscous compaction length, δ, is determined by λ_c during the initial phase of sedimentation. Thus, a comparison of models for different λ_c values illustrates that the porosity wavelength has little dependence on δ, but is dependent on l. The shorter time scale of the $l=500$ m models causes the models to evolve toward a quasi-stationary state, with the compaction front at a greater depth, more rapidly than the $l=1500$ m models. Because the fluid pressure gradient is more nearly hydrostatic in large waves than it is in small waves, large-amplitude wave trains propagate more rapidly. However, the wave trains propagate more slowly than the associated compaction front, with the exception of low-permeability, long viscous e-fold length model in which the wave front is constrained by the compaction front.

toward a hydrostatic gradient (at $t=3.7$ My and $z=1.5$–2.8 km, Fig. 12b). The domain broadens, and the fluid overpressures increase with time as fluid is supplied from below and hydraulic diffusion and pore dilation propagate the domain upward into the obstruction. The increase in pore pressure leads to conditions such that the rate of pore dilation, integrated over the depth interval where supralithostatic pressures maintain, exceeds the volumetric fluid flux from below, whereupon effective pressures at the base of the domain become positive and cause the porosity to collapse (at $t=3.7$ My and $z=2.1$–3.3 km, Fig. 12b). When the porosity collapses to values comparable to the porosity of the obstruction, the fluid fluxes into and out of the porous domain balance each other, and the domain ceases to grow. Thereafter, the effect of pore dilation at the top of the domain, together with pore compaction at a greater depth, is to propagate the region of dilated porosity upward as a wave of anomalous porosity. The collapsed porosity beneath the initial wave forms an obstruction to compaction-driven fluid expulsion at greater depth, causing the nucleation of a second wave. This mechanism effectively propagates the initial obstruction downward against the direction of fluid flow and results in the formation of a wave train that extends over the entire depth interval of hydraulically limited compaction. The ultimate effect of this process is to form a series of sill-like fluid compartments within which the fluid is overpressured, but the fluid pressure gradient is hydrostatic.

The amplitude of porosity waves, the analogy of secondary porosity in sedimentary fluid compartments, is proportional to the difference between the porosity of the flow obstruction and the unobstructed porosity at a greater depth (e.g. Richter and McKenzie, 1984). Large-amplitude porosity waves would therefore be favored by rapid burial of low-permeability sediments, i.e. large ϕ_{ss}, followed by a sedimentary hiatus. The porosity of the obstruction formed by the compaction front is largely independent of permeability, unlike the porosity at a greater depth, therefore both the absolute and relative amplitude of the waves increases as sediment permeability is decreased. The porosity beneath the compaction front is a non-linear function of the ratio of burial rate to initial sediment permeability [Eq. (46)]. Consequently, a relatively small increase in sediment permeability leads to a substantial reduction in amplitude (Fig. 12a).

The length scale, L, over which an effective pressure gradient can be maintained in viscously compacting sediment determines the flow instability wavelength. For thermally activated compaction, L has been shown (Connolly and Podladchikov, 1998) to be either l or the local viscous compaction length (δ, e.g. McKenzie, 1984), with the shorter tending to dominate. For the formulation adopted here, the local viscous compaction length is (Connolly and Podladchikov, 1998)

$$\delta=\sqrt{\frac{k\zeta}{\mu\phi}}. \tag{59}$$

Substituting Eqs. (21) and (23) into Eq. (59), and taking ϕ_{ss} as characteristic of the fluidized porosity yields:

$$\delta=\frac{\lambda_{\mathrm{c}}}{z_{\mathrm{c}}}\left(n(n-1)\exp\left(\frac{z+z_{\mathrm{c}}}{l}\right)\right)^{-1/2} \tag{60}$$

Thus, the counterintuitive result that wavelength is a weak function of k_{r} (Fig. 12) is explicable because δ is only weakly dependent on permeability through z_{c}. The decay of δ with depth increases its influence, resulting in a reduction in wavelength that is more pronounced for short l.

Unlike the compaction front, which forms under the influence of the surface boundary conditions, subjacent porosity waves are effectively isolated from the surface boundary by the compaction front. Therefore, there is no reason for the waves to evolve to a stationary steady state, although such a state does exist for the case that the waves propagate with a velocity identical in magnitude but opposite to that of the matrix. Excepting this case, the matrix viscosity varies as a wave changes its position relative to the surface precluding the attainment of a true steady state. Despite this effect, insight into wave propagation is gained by considering the steady-state solution for large-amplitude waves in a matrix without depth-dependent shear viscosity, i.e. $l=\infty$. As the fluid pressure gradient necessary to sustain a fluid flux varies inversely with permeability and therefore ϕ^n, the stipulation of large amplitude waves permits the assumption that $\nabla p_{\mathrm{e}}=\Delta\rho g$ over a large fraction of the wave. For example, if the maximum porosity ($\phi_{\max}$) is four times the minimum ($\phi_{\min}$), then ∇p_{e} is $0.98\Delta\rho g$ at $\phi_{\max}$ and $0.88\Delta\rho g$ at $0.5\phi_{\max}$ if $n=3$. Expanding the substantial derivative of porosity in Eq. (9) and taking the partial time derivative of porosity as zero, in conjunction with Eq. (23) (with $m=1$), the steady state is a Gaussian solitary wave

$$\phi'=\exp\left(-\frac{1}{2}\left(\frac{z-z_0}{\lambda}\right)^2\right)\text{ with }\lambda=\sqrt{\frac{-v_\phi\eta}{\Delta\rho g}} \tag{61}$$

where $p_{\mathrm{e}}=0$ at the wave center (at $z=z_0$) and $\phi'=\phi/\phi_{\max}$. If the wavelength λ is comparable to the viscous compaction length δ [Eq. (59)], then the velocity required by Eq. (61) is approximately

$$v_\phi=-\frac{k\Delta\rho g}{\mu\phi} \tag{62}$$

identical to the velocity necessary for fluidization at the maximum porosity ($\phi_{\max}$) of the wave. Wave trains formed by an obstruction to a region of uniform porosity cannot become attenuated with time (Spiegelman, 1993; Connolly and Podladchikov, 1998), which implies that Eq. (62) is an upper limit for waves formed in response to a sedimentary hiatus. The assumption that the pressure gradient is equal to $\Delta\rho g$ maximizes the deformation rate within the wave and therefore also gives Eq. (62) as an upper limit on the velocity of smaller waves. Because the pressure gradient at the wave center varies as $(\phi_{\max}/\phi_{\min})^n$, low sediment permeabilities, which result in a large flow obstructions, lead to more rapidly propagating waves, an effect demonstrated by the numerical models (Fig. 12).

The stationary state of porosity waves in a matrix with finite l, is conveniently described in terms of dimensionless depth $z'=(z-z_0)/l$ relative to the wave center at z_0

$$\phi'=\exp\left(\frac{(1-z')e^{z'}-1}{\lambda'^2}\right) \tag{63}$$

where $\lambda' = \lambda/l$ with λ as in Eq. (61), which is identical to the steady-state wavelength of the compaction front at $z_0 = z_c$ and varies with depth as

$$\lambda = \lambda_c \exp\left(\frac{z_c - z}{2l}\right).$$

The stationary states (Fig. 13) show that the constant viscosity solution [Eq. (61)], whereby $\lambda \sim \delta$, is appropriate if $\lambda/l < 0.1$. However, large values of λ/l induce strong asymmetry. That this asymmetry is not well developed in the transient models (Fig. 12, where $\lambda/l = 2$–6 for $l = 1500$ m and $\lambda/l = 8$–80 for $l = 500$ m) reflects that the waves propagate in the direction in which the asymmetry is pronounced. Thus, transient wave shapes are determined primarily by the compaction of the relatively weak sediment below the wave center and are reasonably approximated by the constant viscosity solution. Since the width of the compacting region varies as $(\lambda/l)^{1/2}$ (Fig. 13), but transient velocities decay exponentially (Fig. 12), wave velocities are reasonably estimated from Eq. (62) by assuming $\lambda = l$

$$v_\phi = -\frac{l^2 \Delta\rho g}{\eta_r} \exp\left(\frac{z - z_r}{l}\right). \qquad (64)$$

In distinction to the constant viscosity limit, this approximation indicates that wave velocities are independent of permeability and a strong function of depth and l, a limit realized in the numerical models. This result suggests that rheology, rather than hydrology, dominates the growth and propagation of the flow instabilities. Neglecting the weak dependence of the pressure gradient on amplitude in large waves, the effective pressure responsible for wave propagation is only a function of depth relative to the wave center because of the effective isolation of the fluid within the wave from the surface boundary. In contrast, within the compaction front, the effective pressure is a function of the absolute depth. From Eqs. (29) and (64), this difference causes the compaction front to propagate with a velocity $\sim z/l$ times that of a porosity wave at the same depth. This behavior is manifest in models where wave trains that initiate at a depth $z/l > 1$ (i.e. the dashed and thin solid curves, Fig. 12) initially propagate slower than the compaction front, leading to an initial broadening of the flow obstruction formed in the wake of the compaction front.

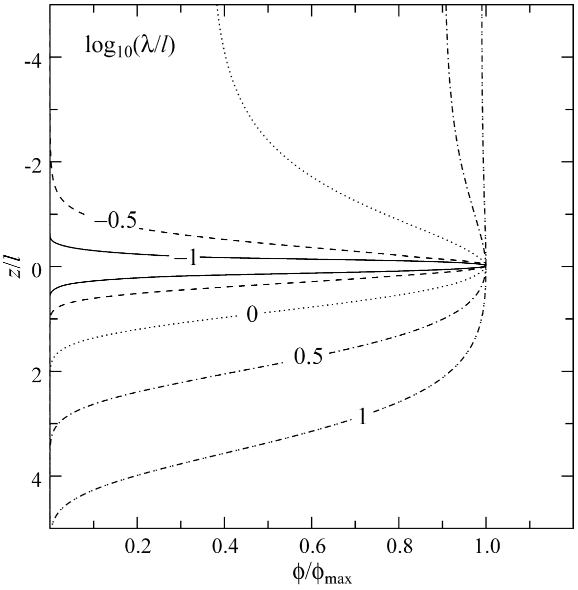

Fig. 13. Stationary states for large ($\phi_{max}/\phi_{min} > \sim 2$) porosity waves as a function of λ/l for $m = 1$. The depth coordinate is chosen so that $p_e = 0$ at $z = 0$. If $\lambda/l < \sim 0.1$, then waves develop on a scale that is short compared to the viscous e-fold length. Consequently, the variation in viscosity is small over the wave length scale, and the Gaussian stationary state of the constant shear viscosity model is realized. Attainment of the stationary state for finite l, requires that the phase velocity of the wave is exactly opposite the sediment velocity. This condition is unlikely to be met, but results in a weak porosity depth dependence above the wave center at $z = 0$. Upward propagation of transient waves tends to suppress the development of this asymmetry, leading to the formation of Gaussian waves at large λ/l, as illustrated by the numerical results (Fig. 12), for which $\lambda/l = 35.4$ ($l = 500$ m) and $\lambda/l = 1.67$ ($l = 1500$ m).

Numerical and mathematical studies of porosity waves have shown that in a constant viscosity matrix, the one-dimensional sill-like waves obtained here are unstable and decompose into spherical waves (Scott and Stevenson, 1986; Wiggins and Spiegelman, 1995). However, in thermally activated compaction, upward strengthening stabilizes the one-dimensional wave geometry provided $\delta/l < 1$ (Connolly and Podladchikov, 1998), the case that appears relevant to sedimentary compaction.

4.2. Porosity waves in a yielding viscous matrix

Negative effective pressures ($\sim -l\Delta\rho g/2$) are an inescapable result of flow instability and porosity wave nucleation in viscously compacting sediment. Although, the existence of 'secondary' porosity induced by hydrocarbon migration (e.g. Szalay, 1988) is evidence that negative effective pressures are possible, it is improbable that sediments support large negative effective pressures without failing by hydrofracturing or other yielding mechanisms. To account for yielding in numerical calculations, the shear matrix viscosity was reduced by three orders of magnitude at effective pressures below the yield threshold, taken as zero effective pressure. The factor is arbitrary, but does not sensibly influence results provided the matrix viscosity during decompaction is at least an order of magnitude lower than the viscosity during compaction.

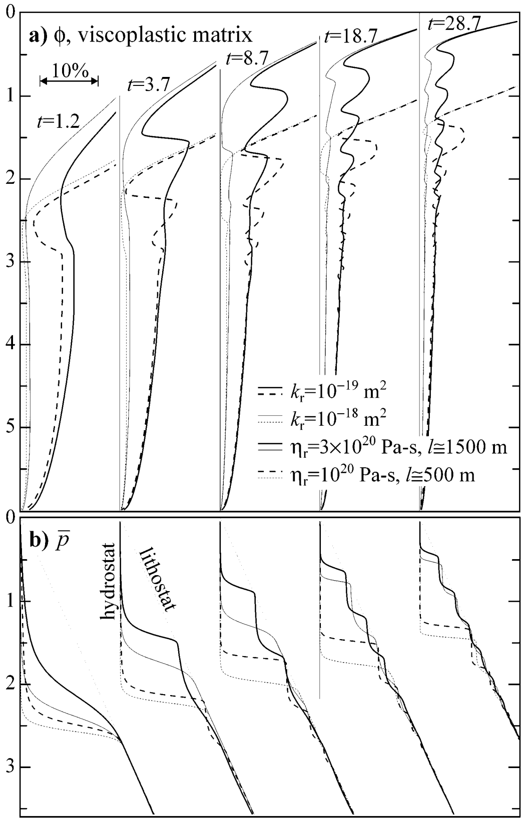

Fig. 14. Numerically calculated porosity (a) and overpressure (b) profiles, for viscous sediment with yielding at zero effective pressure, at approximately exponentially increasing time intervals after the cessation of steady sedimentation, with the same parameters as in Fig. 12. In a yielding matrix, porosity waves that initiate in response to the cessation of sedimentation propagate faster and have wavelengths roughly half that of waves in the simple viscous case. Yielding reduces the overpressure necessary for wave propagation, resulting in step-like fluid pressure profiles similar to those of compartmentalized sedimentary sequences. Porosity waves that propagate in a viscoplastic matrix without losing fluid volume are characterized by a shock front, below which the porosity decreases with depth, as in viscous waves. In the latter part of the model evolution, the waves lose fluid across the compaction front and decay in both amplitude and wavelength.

The porosity waves generated in a yielding matrix (Fig. 14) differ fundamentally from the simple viscous case only in that the mean fluid pressure within the waves is sublithostatic. This has the effect of producing a step-like fluid pressure distribution with depth, a feature characteristic of compartmentalized sedimentary sequences (e.g. Hunt, 1990). In detail, plastic yielding reduces the symmetry and size of the waves, and accelerates the drainage of fluid trapped beneath the compaction front, but does not fundamentally alter the development or scaling of flow instabilities. That yielding does not cause waves to dissipate may be counterintuitive, but is explicable in the context of the conceptual model discussed earlier for viscous waves. For the case of true plastic yielding ($\zeta=0$) at zero effective pressure, any occlusion of the porosity underlying the compaction front would be propagated upward, producing a profile characteristic of fluidized compaction. However, if the sediment has a finite resistance to yielding at zero effective pressure, then the occlusion in the porosity formed consequent to a sedimentary hiatus must cause a small increase in the maximum porosity within the fluidized region beneath the compaction front (heavy solid curve for $t=1.2$ My at $z=2.8$ km, Fig. 14a). Fluid fluxes in this region are greater than in the underlying porosity, which must eventually collapse by viscous compaction ($t=3.7$ My at $z=1.5$–3 km Fig. 14a), creating a wave of porosity in a manner exactly analogous to the simple viscous model (Fig. 12). In a yielding matrix, wave propagation is limited only by the rate at which viscous compaction can drive fluid flow to the wave front and, because dilation is more rapid than compaction, this front is sharper than in the viscous case. The maxima in fluid pressure and porosity are thus more nearly coincident in a viscoplastic wave and, provided the condition for plastic yielding is near zero effective pressure, must be smaller and propagate more rapidly than waves in a viscous matrix. A consequence of this acceleration is that the numerical models for the viscoplastic case illustrate a more advanced evolution in which the waves have begun to decay as a result of interaction with the compaction front. Decay occurs when the wave train impinges on the compaction front and raises the intervening porosity to a value large enough to accommodate the fluid flux from beneath the compaction front. Thereafter, wave propagation cannot occur without loss of fluid mass. In the viscoplastic case, viscous compaction caused by the loss of fluid mass is slow compared to the propagation of the wave by plastic dilation so that the maximum in porosity is displaced behind the wave front, resulting in wave forms that are superficially similar to the viscous case. The decay is asymptotic with time, and, even with accelerated drainage caused by yielding, porosity waves may be retained on a 100 My time scale.

Similar results are obtained if yielding is accounted for by the pseudoelastic term in the compaction equation [Eq. (9)], provided $De>1$, (Connolly and Podladchikov, 1998). Step-like pressure–depth profiles can also be obtained from viscous models if compaction becomes less efficient with decreasing porosity, as observed for non-Newtonian rheologies [Eq. (24)], Ashby, 1988).

4.3. A numerical model of devolatilization-induced flow instability

Two potential difficulties in relating the viscoplastic porosity wave model to basin processes are posed by the time required to generate a flow obstruction following a perturbation to steady sedimentation, and by the large value of κ (i.e. low k or high q_s) required to retain sufficient fluid below the compaction front. Devolatilization reactions offer a mechanism of producing both fluid and porosity below the compaction front without requiring extraordinary permeabilities or sedimentation rates. Moreover, devolatilization is capable of producing a depth interval of finite porosity bounded by fully compacted sediments on a time scale that is limited only by reaction kinetics. Such a scenario is analogous to the generation of a flow obstruction with infinite relative amplitude purely by viscoplastic compaction, but without the restrictive time scale. In terms of the depth interval of interest here, the dehydration of clay minerals (smectite and kaolinite), diagenetic decarbonation, and kerogen decomposition that occur at $T\sim 423$–573 K are potentially important fluid sources (e.g. Clayton et al., 1990; Bjørlykke, 1993). To account for the effects of such reactions in a numerical model, the right-hand sides of the dimensional forms of Eqs. (50) and (51) were modified by the addition of source terms for the volumetric production of fluid (S_f) and porosity (S_ϕ). At the low confining pressures characteristic of sedimentary basins, devolatilization generally occurs such that $S_\phi < S_f$. Under poorly drained conditions, incipient diagenetic devolatilization therefore tends to generate overpressures (e.g. Hubbert and Rubey, 1959; Wong et al., 1997), a potentially important effect in sedimentary environments (e.g. Szalay, 1988; Clayton et al., 1990; Hunt, 1990). In a viscous matrix, such overpressures affect local deformation, but the ratio S_ϕ/S_f and the dependence of reaction kinetics on fluid pressure are of minor consequence to the development of flow instabilities that ultimately modulate the overpressure on the compaction length scale (e.g. Connolly, 1997). We therefore discount these effects and assume equilibrium devolatilization with $S_\phi = S_f$. For simplicity, burial is isothermal, and there are no pressure effects on the temperature of devolatilization so that devolatilization occurs across eustatic reaction fronts. The source term, S_f, is then expressed in terms of the sediment velocity and reaction front width (w)

$$S_f = f\frac{v_s}{w} \tag{65}$$

where f is the volume of fluid generated per unit volume of rock. The values f of employed here (2.9–5.8%, i.e. 1–2 wt%) are plausible, given that diagenetic volatile budgets in sedimentary basins may exceed 20 vol% (e.g. Bjørlykke, 1993). Because a narrow reaction front generates a large relative flow obstruction that amplifies flow instability, the front width is a potentially important factor if it is significantly less than the compaction length scale. To provide conservative models for the generation of porosity waves by devolatilization, the reaction front is taken to be relatively wide, i.e. 500 m. Broad reaction fronts are also consistent with the high thermodynamic variance of low-temperature devolatilization processes (e.g. Connolly, 1997). Heterogeneity in fluid production on the porosity wavelength scale has little impact, but to simulate larger-scale heterogeneity, the numerical models are configured with two sources separated by a 1 km depth interval. There is evidence that hydrocarbons currently trapped in secondary porosity at ~3 km depth in the Pannonian Basin have migrated from depths of ~6 km (Clayton et al., 1990), but hydrocarbon generation typically commences at somewhat shallower depths. Although the depth of the upper model source (5.5 km) is perhaps excessive, it is chosen to illustrate the dynamics of the flow instabilities. Models with shallower sources give similar results, but wave interactions obscure the factors controlling the evolution of the instabilities.

The numerical models (Fig. 15) demonstrate that devolatilization in conjunction with viscoplastic compaction is capable of producing a compartmentalized sedimentary sequence from homogeneous initial conditions with plausible sedimentary parameters. In distinction to the previous models of waves induced entirely by compaction, in which the sediment velocity during wave initiation was zero, in the devolatilization models, the waves must propagate against the downward movement of the matrix during sedimentation. Consequently, a requisite for wave nucleation is that waves propagate upward more rapidly than the rate at which the sediment is buried. Two factors favor wave nucleation and detachment in the short viscous e-fold length model: (1) lower sediment viscosity at depth increases the wave velocities [Eq. (64)]; and (2) less reaction is required to generate the porosity of the relatively small waves. Indeed, in the long e-fold length

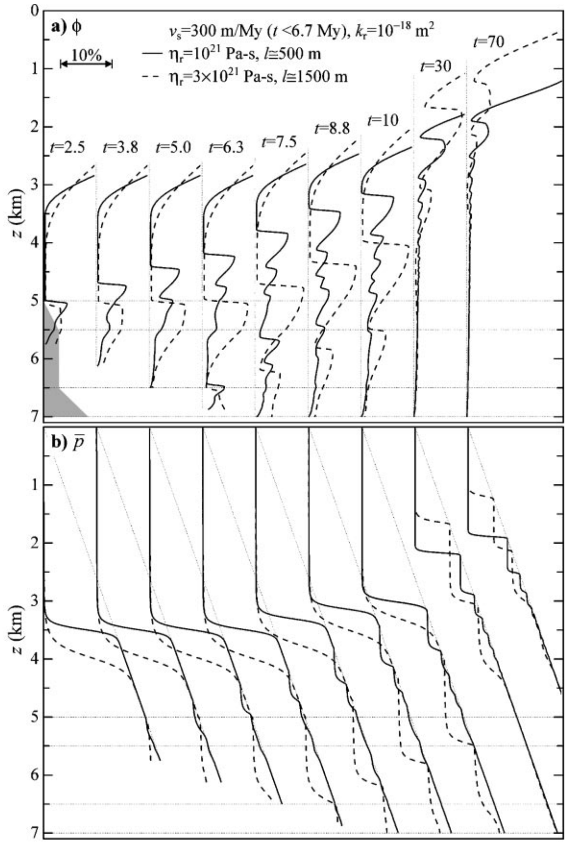

Fig. 15. Porosity (a) and overpressure (b) profiles for models of devolatilization in a viscoplastic sediment matrix, as a function of time following the onset of devolatilization. The calculations were made for constant Q (20 or 60 kJ/mol) with ∇T= 50 K/km and other parameters as indicated or in Table 1. Reaction fronts are indicated by thin dotted horizontal lines, upper and lower reactions release 1 and 2 wt% water respectively, and devolatilization ceases with the end of sedimentation at $t=6.7$ My. The shaded gray field at $t=2.5$ My shows the distribution of porosity that would be generated by the reactions if compaction did not occur. The models assume isochoric devolatilization. Pressure effects normally associated with diagenetic devolatilization would enhance development of porosity waves. In distinction to flow instabilities that develop entirely from compaction processes (Figs. 12 and 14), initiation of porosity waves by devolatilization occurs on a short time scale and does not require extraordinary sediment velocities or permeability. The profiles at $t=30$ and 70 My demonstrate that porosity waves are capable of forming fluid compartments that would persist in inactive basins.

model, the waves only become large enough to propagate beyond the reaction front at a model time almost coincidental with the cessation of sedimentation. Thus, high sedimentation rates may suppress the wave nucleation, but even in such cases, devolatilization results in a domain of occluded porosity from which waves nucleate once the sedimentation rate decreases. Although the models were not constructed to simulate the Pannonian basin, the wave velocities of the short e-fold length model are consistent with the rates of vertical fluid migration ($\sim$250–500 m/My) inferred from geochemical evidence (Clayton et al., 1990) and the development of secondary porosity (Szalay, 1988). Heterogeneous fluid production on a length scale $>l$ can lead to more complex interactions between waves than is the case for coherent waves generated from a single obstruction such as the compaction front. The short viscous e-fold length numerical model (Fig. 15) provides an example of such interactions when the large amplitude wave from the deeper source gains fluid at the expense of the smaller and more slowly propagating waves that it overtakes. This mechanism causes fluid generated by isolated sources to be swept into larger porosity waves that accumulate beneath the compaction front. Thus, multiple fluid sources at depth have the same ultimate effect as a homogeneous source in that they produce a sequence of porosity waves that diminish with depth. As in the case of wave trains generated entirely by compaction, the wave trains generated by devolatilization slow and decay asymptotically as they approach the compaction front and are therefore features that could be retained in inactive basins on a time scale in excess of 100 My.

5. Discussion and conclusion

Thermal activation of precipitation–dissolution processes in sedimentary basins can cause fluid overpressure to develop over a narrow depth interval comparable to the viscous e-fold length. This interval is marked by a rapid decrease in sediment porosity . The observation that, despite sources of natural variability, overpressure development occurs at the same depth in many sedimentary basins is explicable if the viscous e-fold length is small in comparison to the normally pressured depth interval. To quantify this behavior we have explored steady state solutions to the viscoelastic compaction equations. The solution for the viscous limit can be inverted to identify porosity profiles consistent with the viscous model and to constrain its parameters. The approach is distinct from typical fitting procedures in that it exploits the peculiar curvature of viscous compaction profiles. The linear viscoelastic model is remarkably successful in reproducing the porosity profiles observed in the Pannonian basin with three parameters: the viscous e-fold length; λ_c, the length scale of the viscous compaction front in the limit of no thermal activation; and the pseudoelastic pore compressibility. For both the pelitic and psammitic Pannonian lithologies, the activation energies are similar to those inferred for pressure solution creep in quartzites (Angevine and Turcotte, 1983; Rutter, 1983; Shimizu, 1995; Schneider et al., 1996). Effective sediment viscosities from the inverse model are consistent with estimates derived from geodynamic considerations of subsidence and diapirism (Gratz, 1991; Poliakov et al., 1993a). Although success is not proof of validity, the ability of the viscoelastic model to reproduce natural trends with physically meaningful parameters lends the model credence. However, deviations from near surface porosity trends can be explained in the context of pseudoelastic models by a non-linear increase in the mean stress with depth, due to sediment induration and tectonic stresses (e.g. Shi and Wang, 1986). Such models have been applied to describe the fluid pressure evolution of the Pannonian Basin (Van Balen and Cloetingh, 1994). It is noteworthy that the porosity profile of the Pannonian basin Hod-I borehole (Szalay, 1988) shows no significant deviation from the normal pseudoelastic trend. This difference may be attributed to the effects of overpressuring as a result of hydrocarbon generation, but there is little reason to expect that effective viscous properties deduced from a single profile should be valid in general. It is therefore premature to ascribe a general significance to the viscous parameters inferred here.

Although non-Newtonian viscous behavior is tractable by the methods employed here, our analytical formulation assumes a linear stress dependence. While there is evidence that pressure solution creep is Newtonian (e.g. Rutter, 1983), the stress dependence of macroscopic precipitation–dissolution compaction mechanisms (Qin and Ortoleva, 1994; Bjørkum, 1995) is not necessarily linear, and some lithologies are known to compact with a non-linear stress dependence (e.g. carbonates and evaporites, Spiers and Schutjens, 1990; De Meer and Spiers, 1995). Non-linear viscous compaction would generally strengthen porosity variation with depth and would be in many respects indistinguishable from the effect of thermal activation. A potentially important exception would be a non-linear viscous rheology with a negative stress exponent. Such a rheology has been proposed as an explanation for the weak stress dependence of sedimentary compaction by precipitation dissolution (B. Den Brok, pers. commun. 1999) and would produce an opposite effect to that of thermal activation.

The characterization of sediment by effective properties is a simplification that obscures natural complexity. Indisputably, lithological heterogeneity must play a role in basin compaction and compartmentalization, but these effects are superimposed upon the patterns that result from the compaction process. Our goal here was to quantify these patterns. Rheologically controlled compaction leads to a reduction in permeability that causes a transition, that is analogous to the top seal of an overpressured sedimentary sequence, to a hydraulically limited compaction regime characterized by fluid pressures comparable to the sediment load. Perturbations to a regime of steady sedimentation that result in a reduction in sedimentation rate cause the compaction front to propagate upward, forming an interval of lowered porosity that acts as an obstruction to fluid flow. This obstruction initiates flow instability that is manifest by porosity waves that propagate information about the obstruction downward against the direction of fluid flow, resulting in compartmentalization of the hydraulically limited compaction regime. The quasi-steady-state model is simplified in that we assume that the transition to hydraulically limited compaction occurs in the viscous limit. Elsewhere (Connolly and Podladchikov, 1998), we have shown that for small, but finite, *De*, the viscoelastic stationary state is characterized by wave-like oscillations in porosity and effective pressure that decay with depth. Should such values of the Deborah number be relevant at the depth of the transitional regime, compartmentalization would be an intrinsic feature of the steady state.

For plausible sedimentary parameters, the length scale of the porosity waves, i.e. compartments, is determined largely by the viscous e-fold length ($\sim$0.5–1.5 km), but wavelength is also weakly dependent on local sediment viscosity, which decays downward. Wave amplitude is proportional to the reduction in the sedimentation rate that initiates flow instability, such that rapid sedimentation followed by a sedimentary hiatus is the optimal scenario for compaction-induced compartmentalization. Although porosity waves propagate upward with velocities that are an exponential function of depth, the waves are constrained by the compaction front. Thus, waves that form at depth tend to coalesce into larger, essentially eustatic, waves immediately beneath the compaction front. A discrepancy between the viscous porosity wave model and natural fluid compartments is that the mean fluid pressure within porosity waves is almost lithostatic, whereas in natural compartments, fluid pressures approach lithostatic. This type of fluid pressure distribution is produced by porosity waves if yielding is incorporated into the rheological model. The yield mechanism has little influence on the time and length scales of compartmentalization because fluid expulsion remains limited by the viscous compaction. In one-dimensional compaction, the effect of yielding on the porosity–permeability relationship is immaterial because the direction of fluid flow is fixed. More generally, the yield mechanism may influence porosity wave geometry. Thus, the one-dimensional geometric model in which flow instabilities take the form of horizontal sill-like structures might be justified by fracturing at sublithostatic fluid pressure (Simpson, 2000), whereas ideal plastic yielding promotes channeling instabilities and creates more complex structures (Connolly and Podladchikov, 1998). Viscous rheology is not a necessary condition for the development of flow instabilities during hydraulically limited compaction. However, the flow instabilities that would develop in an elastic or pseudoelastic sediment matrix have no intrinsic length scale (Rice, 1992; Connolly and Podladchikov, 1998). The viscous model is therefore more satisfying in that the formation of both a top-seal and subjacent fluid compartments is explicable as an inherent feature of the compaction process.

Devolatilization reactions are sources of both fluid and pore volume that vary as a function of time and depth. If such a reaction commences at depth, the process creates a domain of elevated fluid-filled porosity from which flow is obstructed by the super- and subjacent unreacted sediment. This situation is essentially identical to that responsible for initiating porosity waves in response to perturbations in the sedimentation rate. Unlike the nucleation of waves due entirely to burial and compaction, initiation of large amplitude waves by devolatilization does not require rapid sedimentation of low-permeability materials and appears plausible in view of sedimentary volatile budgets.

Porosity waves are an episodic flow mechanism that may give rise to fluid fluxes that deviate significantly from those anticipated by consideration of uniform Darcyian flow. In sediment with thermally activated viscosity, the waves are an efficient fluid transport mechanism at depth, but become a trapping mechanism at shallower depths as viscosity increases. Although our parameterization assumes that porosity is uniformly distributed on a grain scale, this is not a requisite for the wave mechanism. Given that fracture permeability is a non-linearly increasing function of fracture width, the instability responsible for wave formation must also exist within domains of interconnected fractures. In distinction to fracture propagation, the direction of compaction driven fluid flow is determined by the mean stress gradient. By assuming that this gradient is positive, we have restricted the direction of fluid flow and wave propagation to be upward. Far-field tectonic conditions may result in local inversions of the normal gradient (Petrini and Podladchikov, 2000). An inversion such that $\nabla\bar{\sigma} < \rho_f g$ has particularly interesting implications for fluid migration in sedimentary basins because it would cause buoyant fluids to be driven downward by compaction processes, but would not otherwise affect flow mechanisms. The understanding of the interactions between compaction and tectonic processes is therefore a goal worthy of pursuit.

Acknowledgements

We thank S. Schmalholz for historical context. As ever, we are grateful to J.-P. Burg for his patience and editorial skill. Reviews by J. Ridley, R. van Balen and T. Skar improved the presentation and logic of this paper. V.N. Balashov and K. Bjørlykke persuaded us of the importance of yielding.

References

Aharanov, E., Spiegelman, M., Kelemen, P., 1997. Three-dimensional flow and reaction in porous media: implications for the Earth's mantle and sedimentary basins. J. Geophys. Res. 102, 14821–14834.

Al-Shaieb, Z., Puckette, J.O., Abdalla, A.A., Ely, P.B., 1994. Megacompartment complex in the Andarko basin: a completely sealed overpressured phenomenon. In: Ortoleva, P.J. (Ed.), Basin Compartments and Seals. Am. Assoc. Petrol. Geol. Mem., 55–68.

Angevine, C.L., Turcotte, D.L., 1983. Porosity reduction by pressure solution: a theoretical model for quartz arenites. Geol. Soc. Am. Bull. 94, 1129–1134.

Ashby, M.F., 1988. The modeling of hot isostatic pressing. In: Garvare, T. (Ed.), Proceedings HIP: Hot Isostatic Pressing — Theories and Applications. Centek, Lulea, Sweden, pp. 29–40.

Athy, L.F., 1930. Density, porosity and compaction of sedimentary rocks. Am. Assoc. Petrol. Geol. Bull. 14, 1–22.

Audet, D.M., Fowler, A.C., 1992. A mathematical model for compaction in sedimentary basins. Geophys. J. Int. 110, 577–590.

Audet, D.M., 1996. Compaction and overpressuring in Pleistocene sediments on the Louisana Shelf, Gulf of Mexico. Mar. Petrol. Geol. 13, 467–474.

Barcilon, V., Richter, F.M., 1986. Non-linear waves in compacting media. J. Fluid. Mech. 164, 429–448.

Bethke, C.M., 1985. A numerical model of compaction-driven groundwater flow and heat transfer and its application to the paleohydrology of intracratonic sedimentary basins. J. Geophys. Res. 90, 6628–6817.

Biot, M.A., Ode, H., 1965. Theory of gravity instability with variable overburden and compaction. Geophysics 30 (2), 215–227.

Birchwood, R.A., Turcotte, D.L., 1994. A unified approach to geopressuring, low-permeability zone formation, and secondary porosity generation in sedimentary basins. J. Geophys. Res. 99, 20051–20058.

Bjørkum, D.A., 1995. How important is pressure in causing dissolution of quartz in sandstones? J. Sediment. Res. 66, 147–154.

Bjørlykke, K., 1993. Fluid flow in sedimentary basins. Sediment. Geol. 86, 137–158.

Bjørlykke, K., Hoeg, K., 1997. Effects of burial diagenesis on stresses, compaction and fluid flow in sedimentary basins. Mar. Petrol. Geol. 14, 267–276.

Clayton, J.L., Spencer, C.W., Koncz, I., Szalay, A., 1990. Origin and migration of hydrocarbon gases and carbon dioxide, Bekes Basin, southeastern Hungary. Org. Geochem. 15, 233–247.

Connolly, J.A.D., Thompson, A.B., 1989. Fluid and enthalpy production during regional metamorphism. Contrib. Mineral. Petrol. C102, 346–366.

Connolly, J.A.D., 1997. Devolatilization-generated fluid pressure and deformation-propagated fluid flow during regional metamorphism. J. Geophys. Res. 102, 18149–18173.

Connolly, J.A.D., Podladchikov, Y.Y., 1998. Compaction-driven fluid flow in viscoelastic rock. Geodin. Acta 11, 55–84.

David, C., Wong, T.f., Zhu, W., Zhang, J., 1994. Laboratory measurements of compaction induced permeability change in porous rocks: implications for the generation and maintenance of pore pressure excess in the crust. Pure Appl. Geophys. 143, 425–456.

De Meer, S., Spiers, C.J., 1995. Creep of wet gypsum aggregates under hydrostatic loading conditions. Tectonophysics 245, 171–184.

Dovenyi, P., Horvath, F., 1988. A review of temperature, thermal conductivity, and heat flow data for the Pannonian Basin. Am. Assoc. Petrol. Geol. Mem. 45, 195–234.

Fowler, A.C., Yang, X.-S., 1998. Fast and slow compaction in sedimentary basins. SIAM J. Appl. Math. 59, 365–385.

Fowler, A.C., 1990. A compaction model for melt transport in the Earth's asthenosphere. In: Ryan, M.P. (Ed.), Magma Transport and Storage. Wiley, New York, pp. 3–14.

Fowler, A.C., Yang, X., 1999. Pressure solution and viscous compaction in sedimentary basins. J. Geophys. Res. 104, 12989–12997.

Gratz, A.J., 1991. Solution transfer compaction of quartzites — progress toward a rate law. Geology 19, 901–904.

Gueguen, Y., Dienes, J.K., 1989. Transport properties of rocks from statistics and percolation. Math. Geol. 21, 1–13.

Gueguen, Y., Palciauskas, V.V., 1994. Introduction to the Physics of Rocks. Princeton University Press, Princeton, NJ. 194 pp.

Helle, A.S., Easterling, K.E., Ashby, M.F., 1985. Hot isostatic pressing: new developments. Acta Metall. 32, 2163–2174.

Hubbert, M.K., Rubey, W.W., 1959. Role of fluid pressure in mechanics of overthrust faulting, I. Mechanics of fluid-filled porous solids and its application to overthrust faulting. Geol. Soc. Am. Bull. 70, 115–166.

Hunt, J.M., 1990. Generation and migration of petroleum from abnormally pressured fluid compartments. Am. Assoc. Petrol. Geol. 74, 1–12.

Kooi, H., 1997. Insufficiency of compaction disequilibrium as the sole cause of high pore fluid pressures in pre-Cenozoic sediments. Basin Res. 9, 227–241.

Lundegard, P.D., 1992. Sandstone porosity loss — A 'big picture' view of the importance of compaction. J. Sediment. Petrol. 62, 250–260.

McKenzie, D., 1984. The generation and compaction of partially molten rock. J. Petrol. 2, 713–765.

McKenzie, D., 1987. The compaction of igneous and sedimentary rocks. J. Geol. Soc. Lond. 144, 299–307.

Mann, D.M., MacKenzie, A.S., 1990. Prediction of pore fluid pressures in sedimentary basins. Mar. Petrol. Geol. 7, 55–65.

Neuzil, C.E., 1994. How permeable are clays and shales? Water Resour. Res. 30, 145–150.

Nye, J.F., 1953. The flow law of ice from measurements in glacier tunnels, laboratory experiments and the Jungfraufirn borehole experiment. Proc. R. Soc. Lond. A 219, 477–489.

Oelkers, E.H., Bjørkum, P.A., Murphy, W.M., 1996. A petrographic and computational investigation of quartz cementation and porosity reduction in North Sea sandstones. Am. J. Sci. 296, 420–452.

Palciauskas, V.V., Domenico, P.A., 1989. Fluid pressures in deforming rocks. Water Resour. Res. 25, 203–213.

Petrini, K., Podladchikov, Y., 2000. Lithospheric pressure–depth relationship in compressive regions of thickened crust. J. Metamorph. Geol. 18, 67–78.

Poliakov, A., Cundall, P., Podladchkov, Y., Lyakhovsky, V., 1993a. An explicit inertial method for the simulation of visco-elastic flow: an evaluation of elastic effects on diapiric flow in two- and three-layer models. In: Stone, D.B., Runcorn, S.K. (Eds.), Flow and Creep in the Solar System: Observations Modeling and Theory. Kluwer Academic, Amsterdam, pp. 175–195.

Poliakov, A.N.B., et al., 1993b. Numerical analysis of how sedimentation and redistribution of surficial sediments affects salt diapirism. Tectonophysics 226, 199–216.

Powley, D.E., 1990. Pressures and hydrogeology in petroleum basins. Earth Sci. Rev. 29, 215–226.

Qin, C., Ortoleva, P.J., 1994. Banded diagenetic pressure seals: types, mechanisms, and homogenized basin dynamics. Am. Assoc. Petrol. Geol. Mem. 61, 385–396.

Reiner, M., 1964. The Deborah number. Phys. Today 17, 62

Rice, J.R., 1992. Fault stress states pore pressure distributions and the weakness of the San Andreas fault. In: Evans, B., Wong, T.-F. (Eds.), Fault Mechanics and Transport Properties of Rocks. Academic Press, New York, pp. 475–503.

Richter, F.M., McKenzie, D., 1984. Dynamical models for melt segregation from a deformable rock matrix. J. Geol. 92, 729–740.

Robinson, A., Gluyas, J., 1992. Model calculations of loss of porosity in sandstones as a result of compaction and quartz cementation. Mar. Petrol. Geol. 9, 319–323.

Royden, L.H., Horvath, F., 1988. Early Cenozoic tectonics and paleogeography of the Pannonian and surrounding regions. Am. Assoc. Petrol. Geol. Mem. 45, 1–16.

Rutter, E.H., 1983. Pressure solution in nature, theory and experiment. J. Geol. Soc. Lond. 140, 725–740.

Schneider, F., Potdevin, J.L., Wolf, S., Faille, I., 1996. Mechanical and chemical compaction model for sedimentary basin simulators. Tectonophysics 263, 307–313.

Scott, D., Stevenson, D., 1984. Magma solitons. Geophys. Res. Lett. 11, 1161–1164.

Scott, D., Stevenson, D., 1986. Magma ascent by porous flow. J. Geophys. Res. 91, 9283–9296.

Shi, Y., Wang, C., 1986. Pore pressure generation in sedimentary basins: overloading versus aquathermal. J. Geophys. Res. 91, 2153–2162.

Shimizu, I., 1995. Kinetics of pressure solution creep in quartz, theoretical considerations. Tectonophysics 245, 121–134.

Simpson, G.D.H., 2000. Synmetamorphic vein spacing distributions: characterisation and origin of a distribution of veins from NW Sardinia. J. Struct. Geol. 22, 335–348.

Spiegelman, M., 1993. Flow in deformable porous media. Part 1 Simple analysis. J. Fluid Mech. 247, 17–38.

Spiers, C.J., Schutjens, P.M.T.M., 1990. Densification of crystalline aggregates by diffusional creep. J. Geol. Soc. Spec. Publ. 54, 215–227.

Sumita, I., Yoshida, S., Kumazawa, M., Hamano, Y., 1996. A model for sedimentary compaction of a viscous medium and its application to inner-core growth. Geophys. J. Int. 124, 502–524.

Surdam, R.C., Jiao, Z.S., Martinsen, R.S., 1994. The regional pressure regime in Cretaceous sandstones and shales. In: Ortoleva, P.J. (Ed.), Basin Compartments and Seals. Am. Assoc. Petrol. Geol. Mem., 55–68.

Szalay, A., 1982. Possibilities of the Reconstruction of Basin Evolution in the Prediction of Hydrocarbon Prospects. Hungarian Academy of Sciences, Budapest.

Szalay, A., 1988. Maturation and migration of hydrocarbons in the Southeastern Pannonian Basin. Am. Assoc. Petrol. Geol. Mem. 45, 347–354.

Van Balen, R., Cloetingh, S., 1994. Tectonic control of the sedimentary record and stress-induced fluid flow: constraints from basin modelling. In: Parnell, J. (Ed.), Geofluids: Origin Migration and Evolution of Fluids in Sedimentary Basins. Geol. Soc. Spec. Pub., 9–26.

Wangen, M., 1992. Pressure and time evolution in sedimentary basins. Geophys. J. Int. 100, 601–613.

Wiggins, C., Spiegelman, M., 1995. Magma migration and magmatic solitary waves in 3-d. Geophys. Res. Lett. 22, 1289–1292.

Wong, T.f., Ko, S.c., Olgaard, D.L., 1997. Generation and maintenance of pore pressure excess in a dehydrating system, 2, theoretical analysis. J. Geophys. Res. 102, 841–842.

Zhu, W., David, C., Wong, T.-f., 1995. Network modeling of permeability evolution during cementation and hot isostatic pressing. J. Geophys. Res. 100, 15451–15464.